Research Square

Preprints are preliminary reports that have not undergone peer review.
They should not be considered conclusive, used to inform clinical practice,
or referenced by the media as validated information.

Towards anticancer drug design: Allosteric rewiring of the MDM2–MDMX RING interface by K478R and N448C perturbs structural and functional dynamics

Adeniyi Thompson Adewumi
University of South Africa
Sekele Tshepo Lucas
University of South Africa
Wande Michael Oluyemi
Afe Babalola University
Shadrach Chinecheremeze Eze
Afe Babalola University
Salerwe Mosebi
mosebs@unisa.ac.za

University of South Africa

Article

Keywords: Anticancer drug design, MDM2/MDMX RING heterodimer, RING domain mutations, Molecular dynamics simulation, Protein–protein interaction inhibition, p53 regulation

Posted Date: August 27th, 2026

DOI: https://doi.org/10.21203/rs.3.rs-10475900/v1

License: This work is licensed under a Creative Commons Attribution 4.0 International License.
Read Full License

Additional Declarations: No competing interests reported.

Towards anticancer drug design: Allosteric rewiring of the MDM2–MDMX RING interface by K478R and N448C perturbs structural and functional dynamics

Adeniyi Thompson Adewumi[1], Sekele Tshepo Lucas[1], Wande M. Oluyemi[2], Shadrach C. Eze[2], and Salerwe Mosebi[1]*

[1]Department of Life and Consumer Sciences, College of Agriculture and Environmental Sciences, University of South Africa, Florida Campus, 1710, Roodepoort.

[2]Department of Pharmaceutical and Medicinal Chemistry, College of Pharmacy, Afe Babalola University, Ado-Ekiti, Ekiti State, Nigeria

***Corresponding Authors:**

Professor Salerwe Mosebi*

Tel: +27 011 471 2315

Email: mosebs@unisa.ac.za

Scopus: 8632560900

ORCID: 0000-0002-7028-1712

ABSTRACT

Under normal conditions, the MDM2–MDMX RING complex keeps the crucial tumor suppressor p53 inactive by marking it for degradation. Disrupting this complex with targeted inhibitors like MMRi6 and MMRi64 is a promising targeted anticancer strategy to stabilize p53. However, the exact impact of mutations on the complex and whether they block these inhibitors remains unclear. This study evaluates the impact of MDMX RING mutations (K478R and N448C) on inhibitor binding and structural dynamics. The K478R-MMRi64 yields the most favorable binding free energy (-30.10 kcal/mol), primarily driven by vdW interactions. The K478R/N448C (double mutation) also provides a high binding affinity (-30.05 kcal/mol) among MMRi6 complexes. Hotspots include the PRO444, ARG465, LYS469, and LEU433, identified as the essential residues, that stabilize the inhibitors. K478R–MMRi64 exhibits the highest structural flexibility. Conversely, N448C-MMRi64 exhibits the greatest overall structural stability. The K478R-MMRi64 complex is highly flexible (highest RMSD of 4.1 Å, RMSF = 2.5 Å), while N448C-MMRi64 is most stable (RMSD = 1.9 Å, RMSF = 1.1 Å). The K478R with MMRi64 explores the widest range of shapes, disrupting the overall architecture of the heterodimer. MMRi6 promotes a more compact protein shape, whereas MMRi64 stabilizes a more expanded state. Inhibitor binding alters residue contacts, notably contracting the distance between LYS469 and ARG465 (12.74 Å to 6.44 Å) in K478R–MMRi6), which rewires communication across the RING interface. Therefore, these MDMX mutations can restore p53 anticancer activity; however, because mutations cause varied structural flexibility, personalized inhibitor selection is required to overcome resistance and maximize therapeutic efficacy.

Keywords: Anticancer drug design, MDM2/MDMX RING heterodimer, RING domain mutations, Molecular dynamics simulation, Protein–protein interaction inhibition, p53 regulation.

1.0 INTRODUCTION

Cancer, a deadly disease that causes pathological changes in body physiology, specifically in cell division, has become a significant cause of the global annual death rate (1). Every year, about 19-20 million people die from cancer worldwide (1). Approximately 2 million new cancer cases and 600 thousand cancer deaths are predicted to occur in 2025 in the United States (2). Despite the development of various anti-cancer drugs, which initially showed promise, the emergence of drug resistance through driver mutations or conformational changes in the shape of the active site has now made these drugs ineffective. For example, the $Kras^{G12C}$ inhibitor, adagrasib, doubled the frequency of the Kras G12C mutation in half of NSCLC cases, where this mutation is most prevalent. Other drugs, such as imatinib, nilotinib, and dasatinib, are also resistant to the T315I mutation in the BCR-ABL fusion gene (3).

A major concern in cancer proliferation is the role of the mouse double-minute 2 (MDM2) and MDM4 (MDMX) regulators in ubiquitinating the tumour suppressor p53 protein (4). The p53 protein (**Fig. 1)**, discovered 43 years ago and referred to as the guardian of the genome, is an essential regulator of cell division that inhibits cell growth, thereby preventing tumour development. This protein, also called wild-type p53 (wtp53) (5)(6), is encoded by the TP53 gene and has several biological functions, including regulation of the cell cycle, DNA metabolism, angiogenesis, senescence, apoptosis, and cell differentiation (5). These functions are primarily activated under cellular stress, such as DNA damage, oncogenic signalling, low oxygen levels, or nutrient deficiency (6). Normally, MDM2 and MDM4 act as negative regulators of p53, preventing it from inhibiting the growth of healthy cells. However, it has been established that these regulators, specifically MDM2, are now overexpressed, thereby inhibiting p53 activity and rendering cancer cells resistant to tyrosine kinase inhibitors (TKIs) and other cancer therapies (7).

The TP53 gene, which encodes the p53 protein, is located on chromosome 17 and spans 13 exons and 11 introns (8). The active form of the p53 protein is a homotetramer, made up of 4 identical chains, each consisting of 393 amino acids. Each of these polypeptide chains has different domains, namely: a highly acidic N-terminal transactivation domain (TAD) located at AA (amino acid) 1 – 61; a proline-rich domain (PRD) at AA 64 – 92; a DNA-binding domain (DBD) at AA 96 – 292; a tetramerization domain (TET) linked to the DBD and is located at AA 324 – 356; and a C-terminal regulatory domain (CTD) at AA 364 – 393 (4)(9).

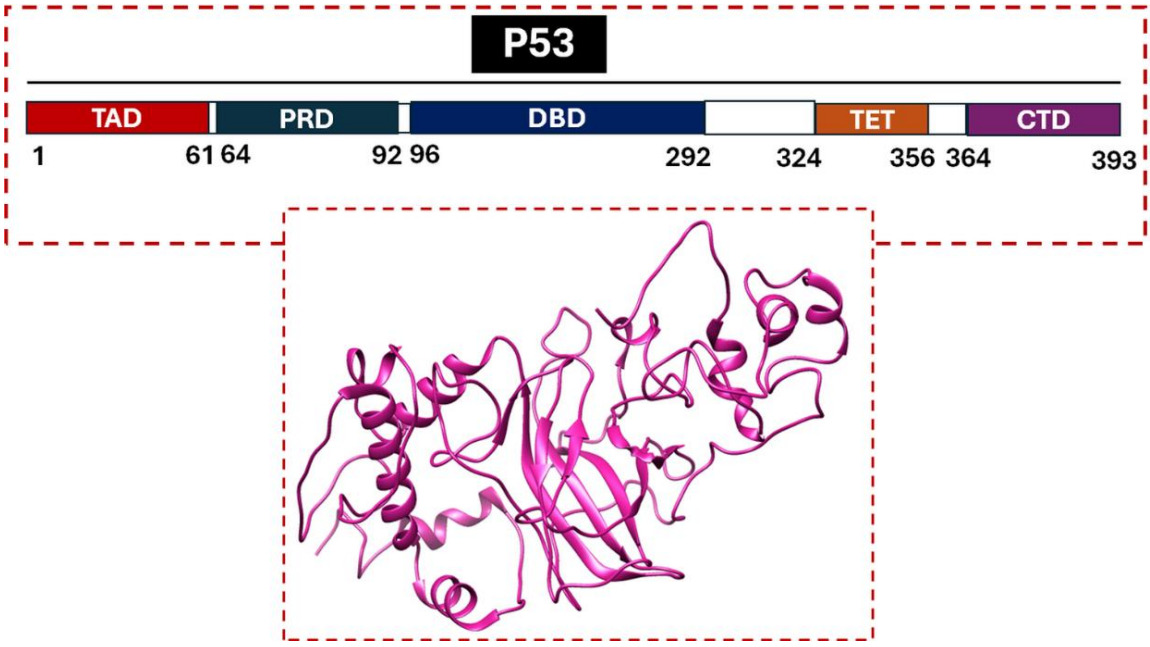


Figure 1. Schematic and structural representation of p53 monomer (p53 structural image generated using UCSF Chimera).

MDM2 is an E3 ubiquitin ligase with a RING domain (Really Interesting New Gene) made up of approximately 50 residues. In contrast, MDMX, which lacks this ligase activity, plays a vital role in supporting MDM2 activity through heterodimer formation. However, it is essential to note that MDM2 homodimer formation can also inhibit p53, although the heterodimer exerts greater p53

suppression. Together, MDM2/X's role in p53 action is to ubiquitinate the protein, marking it for degradation by the 26S proteasome. Ubiquitination is a post-translational modification that occurs through the E1-E2-E3 enzyme pathway. This pathway is activated when an E1 enzyme activates ubiquitin through ATP as a coenzyme, before transferring it to an E2 enzyme. The E2 enzyme, which acts as a conjugating enzyme, transfers ubiquitin directly to the substrate (p53). This action is catalysed by the RING-type E3 enzyme, acting as a ligase (10)(11). It is this peculiarity of MDM2/X to inhibit p53 that has drawn the attention of various researchers to various anti-cancer strategies, including this study.

MDM2 RING and MDMX RING proteins (**Fig. 2**) are structural homologs made up of the following regions: the N-terminus, consisting of a p53 binding domain (transactivation domain, TAD) which contains ~105 AA; a nuclear localisation signal (NLS); a nuclear export signal (NES); an acidic domain; a zinc finger (ZF) domain; and the C-terminus, which contains the RING domain. Although MDM2/X are structurally similar, MDMX lacks an NLS or a NES. These homologs also have lids (intrinsically disordered regions, IDRs) located between AA 1-25 of the N-terminal regions (12)(13). The MDM2–MDMX RING heterodimer plays a pivotal role in p53 ubiquitination and degradation, making it an attractive target for anticancer intervention. Although small-molecule inhibitors such as MMRi6 and MMRi64 have shown promise in targeting the RING-RING heterodimer, the influence of mutations on inhibitor recognition and complex dynamics remains poorly understood.

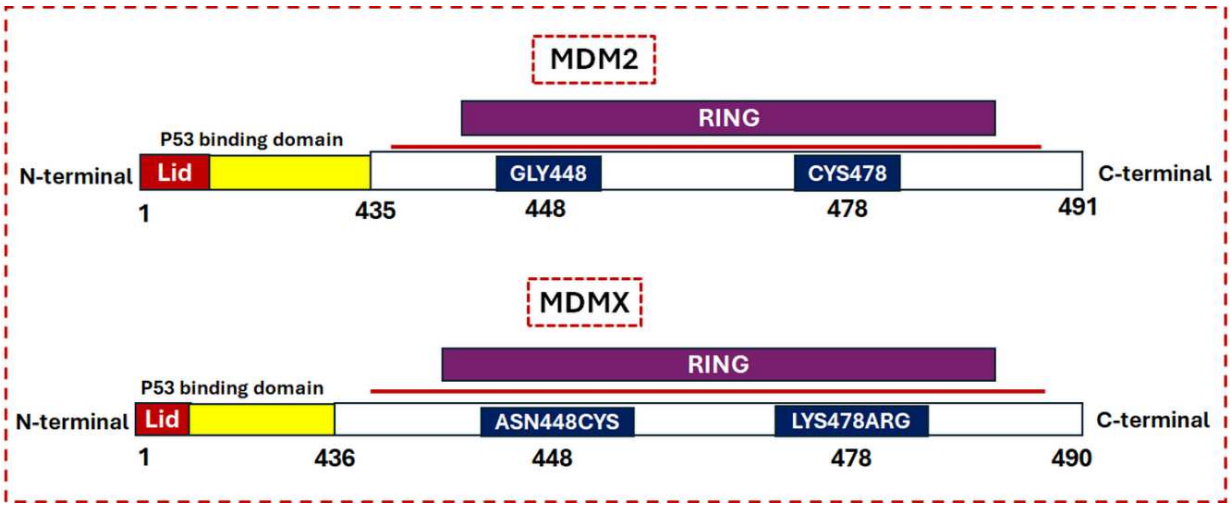


Figure 2. Schematic representation of MDM2/X structures, with the RING domain being the focus. The MDMX representation shows the mutation of ASN and LYS residues at positions 448 and 478 to CYS and ARG, respectively (12).

Xiong et al. (2025) (14), focused on the role of MDMX in assisting MDM2, establishing that the deletion of the MDMX ring domain or the complete removal of MDMX would elevate p53 levels. Other researchers have also focused on identifying inhibitors to block MDM2 activity (7)(11). One study conducted by Lama et al. (2025) (15) showed that MMRi36C, a structural analogue of MMRi36, possesses E3-ligase inhibition properties as well as dissociation properties for the MDM2/X RING domain. Another promising inhibitor, Hinokiflavone (a biflavonoid), was identified through virtual screening and showed the same activity as MMRi36C (16). Other inhibitors, such as MMRi6 and its analogue MMRi64, were shown to be effective in an in vitro study of leukaemia cells (17). However, while these discovered inhibitors have shown promise, they are not FDA-approved (18).

Mutations in the RING domains of MDM2 and MDMX can disrupt their interactions and alter p53 regulation, leading to diverse cellular consequences. These mutations can affect ubiquitin ligase activity, protein-protein interactions, and, ultimately, p53 stability and transcriptional activity.

Studies conducted by Kosztyu et al. 2019 (19) showed that the C449N mutation (done through the exchange of C449 in MDM2 with N448 in the MDMX RING) in the MDM2 chain affected the ability of MDM2 to dimerise with MDMX. They validated this finding by carrying out two other point mutations, C449A and C449S, which did not affect MDM2's ability to bind with MDMX. C462A mutation in MDM2 RING disrupts the RING domain and abolishes its ability to bind to MDMX, leading to embryonic lethality. Moreover, C447S, V457A, and C470A mutations in MDM2's RING domain impair its ability to degrade p53, despite retaining some ubiquitin ligase activity. Other MDM2 RING domain mutations include I440K, I440E, and R479P, which abolish MDM2 ligase activity.

Interestingly, studies carried out by Egorova and Sheng (2014) using a total autoubiquitination assay showed that the K478R point mutation in the MDMX RING domain exhibited weak E3 ligase activity (20). In contrast, the N448C point mutation and the N448C/K478R double mutation showed strong ubiquitination potential, suggesting that these mutations can promote heterodimerization between MDM2 and MDMX.

However, there is limited research on mutating specific residues in either homolog or on how these mutations affect their activities. Therefore, this study aimed to understand the impact of MDMX mutations on the MDM2-MDMX RING domain interface when bound to MMRi6 and MMRi64 inhibitors, which, in turn, can affect its suppressive activity and, subsequently, upregulate the p53 protein. We carried out mutational studies on MDMX in the homology model of MDM2/X using bioinformatics and computational tools, such as computer mutagenesis, molecular docking, molecular dynamics simulations, binding free energy calculations, and interaction network diagrams. We further unravelled the mutational behaviour of the structures and their effects on

p53 inhibition using molecular dynamics simulations, as well as their interactions with the selected ligands.

2.0 METHODOLOGY

2.1 *Retrieval and preparation of MDM2/X heterodimer*

A 3D crystallised tetrameric structure of MDM2/X RING heterodimer domain was retrieved from the RCSB Protein Data Bank (PDB) (https://www.rcsb.org/), with the accession number 2VJE and a resolution of 2.2 Å. UCSF Chimaera (version 1.19)(21) was used to isolate the heterodimeric chain C (MDM2 RING) and chain D (MDMX RING). The "Mutate residue" add-on in the Schrödinger Maestro tool was used to induce mutagenesis of the MDMX RING domain via residue-structure editing. The targeted residues, ASN448 and LYS478, were mutated to CYS and ARG, respectively (**Fig. 3**). The new rotamers, selected and saved in .pdb format for further studies, were those with the least steric hindrance and the highest prevalence.

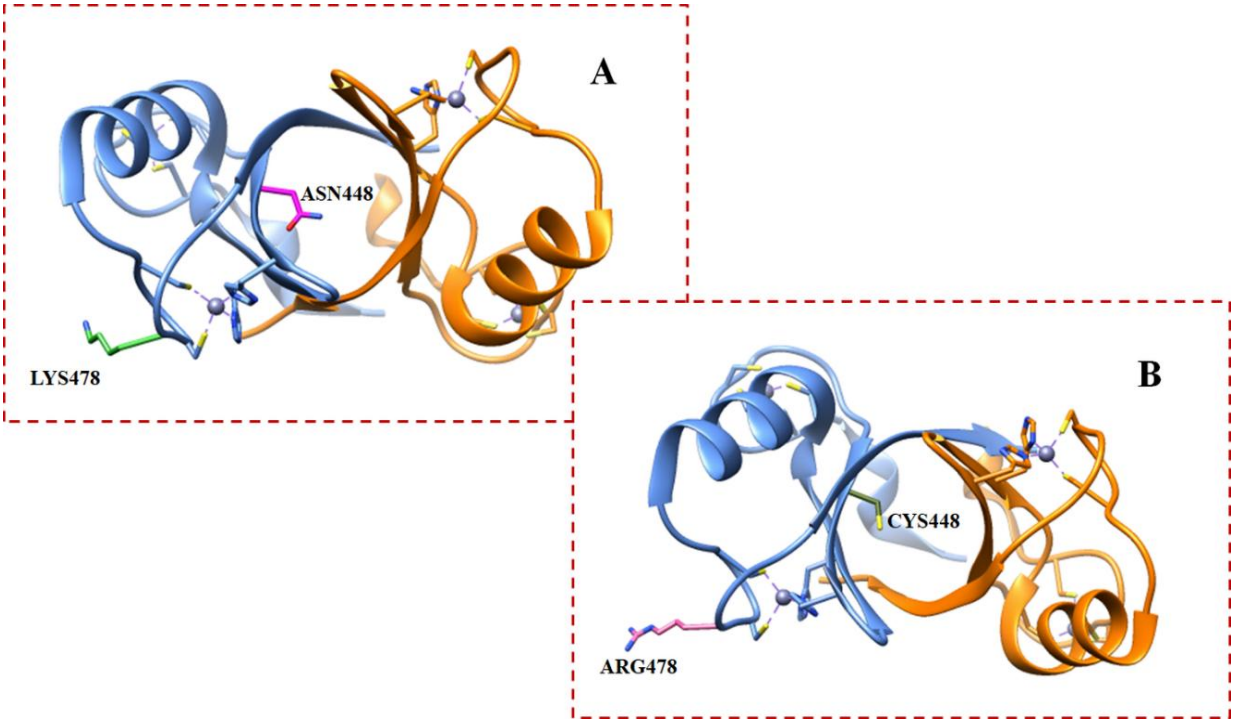


Figure 3. (**A**) Structural representation of MDM2/X (chains C & D) showing the targeted residues: ASN448 (magenta) and LYS478 (lime green). (**B**) Targeted residues have been mutated: CYS448 (dark green) and ARG478 (pink).

Based on structural and functional studies of the MDMX RING domain, the mutants N448C and K478R are considered structural/functional adaptations designed to convert the inactive MDMX RING domain into an active E3 ligase by mimicking the Mdm2 RING domain, rather than simple "contact" (binding) or "structural" (folding) mutants in the traditional sense. N448C (Structural/Stability): The residue N448 is located at the MDMX RING dimer interface. Mutating this to cysteine (C448), which corresponds to C449 in Mdm2, is thought to stabilise the RING dimer structure. K478R (Contact/Activity): The residue K478 in MDMX, which corresponds to R479 in MDM2, is involved in recruiting and activating the ubiquitin E2 conjugating enzyme. Replacing K478 with arginine (K478R) helps restore this catalytic activity.

2.2 *Preparation of ligands and MDM2/X RING heterodimer*

The 2D and 3D structures of the ligands (MMRi6 and MMRi64) were retrieved from the NCBI database (https://www.ncbi.nlm.nih.gov/) and downloaded in the structural data format (SDF). Hydrogen atoms and Gasteiger charges were added using the UCSF Chimera Tool v. 1.19(22) and the ligands were saved as .mol2 files. (23) The receptor was prepared for docking using Chimera and saved in the .pdb format after hydrogen bonds were added and all non-standard residues, such as H_2O, FLC, and SO_4, were deleted. AutoDockTool-1.5.7 was used to import the ligand and receptor, which were converted to PDBQT files to ensure compatibility with AutoDock Vina.

Despite the availability of structural information on heterodimer formation between the MDM2 RING and MDMX RING domains (24), the mechanism remains unclear, as neither the binding

interface nor the active site between the two domains has been reported. The structural basis of the inhibition of the heterodimer activity by small compounds also remains uncertain. However, MDM2/X RING heterodimer interface binding involves three main interaction regions, with the primary one involving the C-terminus of MDM4 binding to the second alpha-helix of MDM2. The C-terminal five residues of both MDM2 and MDMX are crucial for heterodimer formation, with specific residues being particularly important for burying contacts. We therefore extracted the coordinates of the MDM2-MDMX domain and docked MMRi6 and MMRi64 to the receptors by defining the heterodimer interface as the receptor site. The site residues of the MDM2-MDM4 RINGs include MDM2 PRO431, ASN433, ARG444, HIS452, THR455, HIS457, THR463, and LYS467, and MDM4 GLY447, LEU483, ILE485, P476, VAL487, PHE488, ILE489, AND ALA490. In addition, the active sites of the MDM2/X complex were validated by the CASTp server (24). The grid box generated with AutoDock Tools was set to the X, Y, Z coordinates: centre 55.714, 10.615, 39.653, and size 64, 82, 72, respectively. Docking on AutoDock Vina through the Cygwin terminal was performed for each ligand with MDM2/X RING domain receptor. (25) The receptor-ligand interaction, along with the bond distances and angles, was visualised using the BIOVIA Discovery Studio Tool (BIOVIA, 2024).

2.3 *Molecular dynamics simulations*

Molecular dynamics (MD) simulations are preferred over molecular docking because they can be run for much longer to achieve greater stability. (23). The MD simulations were carried out on the Lengau Centre for High-Performance Computing (CHPC) cluster (http://www.ambermd.org) at 200 nm using accelerated AMBER codes contained in the AMBER18 package. (26) The receptor-ligand complexes were described using the AMBER FF18SB force field variant. Partial charges involving the restrained electrostatic potential (RESP) and the General Amber Force Field (GAFF)

were added to the ligands using the Antechamber package. The LEAP module in the AMBER18 code was used to neutralise the systems by adding hydrogen (H^+), sodium (Na^+), and chloride (Cl^-) counterions (27). The complexes were solvated by suspending them in an orthorhombic box of TIP3P water molecules, with a box size of 12 Å. (28) Partial minimisation was carried out for 2500 steps with a restraint potential of 500 kcal/mol $Å^2$, while the full minimisation was performed using the conjugate gradient algorithm for 5000 steps without restraints. The systems were heated gradually using a canonical ensemble (NVT) from 0 to 300 K for 5 ps to maintain a fixed number of atoms and volumes. The systems were fixed with a weak potential harmonic restraint of 10 kcal/mol $Å^2$ and a collision frequency of 1.0 ps-1.(23)

At 300 K, the systems were equilibrated for 1 ns (500,000 steps). The number and pressure of atoms were kept constant using an isobaric isothermal ensemble (NPT) and the Berendsen barostat, respectively (29). The SHAKE algorithm was used to construct the hydrogen atom bond lengths. The coordinates and trajectory's potential were analysed and printed using the AMBER18 GPU PTRAJ module at every 1 ps. Following the MD simulations, the stability and flexibility of the ligand and unliganded systems were assessed using root-mean-square deviation (RMSD) and root-mean-square fluctuation (RMSF), respectively. The principal components (PCA) of the systems were also computed to explore the inter-residual displacement behaviours.

2.4 Thermodynamic calculations

The binding free energies (BFE) (kcal/mol) of the liganded and unliganded systems were determined using the Molecular Mechanics/Generalised Born (Poisson-Boltzmann) Surface Area (MM/GB(PB)SA) calculations. (30) The binding free energy was calculated based on the average of 40000 snapshot frames obtained from a 200 ns trajectory. The BFE (ΔG_{bind}) for each system is based on the energy difference between the receptors and ligands, as shown below. (31):

$\Delta G_{bind} = \Delta G_{complex} - \Delta G_{receptor} - \Delta G_{ligand}$ …….. (i)

$\Delta G_{bind} = E_{gas} + G_{sol} - TS$…… (ii)

$E_{gas} = E_{int} + E_{vdw} + E_{ele}$……... (iii)

$G_{sol} = G_{GB} + G_{SA}$…… (iv)

$G_{SA} = \gamma SASA$……. (v)

Where ΔG_{bind} = summation of the gas phase

E_{gas} = gas-phase energy

G_{sol} = solvation free energy

E_{ele} = Coulomb

E_{int} = internal energy

E_{vdw} = van der Waals energy (32)

3.0 RESULTS AND DISCUSSION

3.1 *Docking binding affinities*

The MDM2–MDMX RING heterodimer serves as the principal regulatory complex responsible for controlling p53 stability through ubiquitin-mediated degradation. While MDMX itself lacks intrinsic E3 ubiquitin ligase activity, its interaction with MDM2 through the RING domains promotes formation of a highly active heterodimer that enhances p53 ubiquitination and degradation compared with MDM2 homodimers (33). Because the structural and dynamic integrity of this heterodimer is essential for efficient p53 suppression, perturbation of RING-domain interactions and allosteric communication networks has emerged as a promising therapeutic strategy for restoring p53 activity in cancer cells (34–36). In the present study, molecular docking was initially employed to evaluate the effects of MDMX RING mutations on

the recognition and binding of the inhibitors MMRi6 and MMRi64 at the MDM2–MDMX heterodimer interface, using the protein-ligand docking method with the AutoDock Vina protocol.

Docking analysis revealed mutation-dependent variations in ligand affinity, suggesting that substitutions within the MDMX RING domain alter the physicochemical environment of the heterodimer interface. The inhibitors MMRi6 and MMRi64 were docked, and their binding affinities to the MDM2/X RING domain complex were identified. The docking was carried out on different systems of the MDM2/X complex: wild-type (WT), K478R point mutation, N448C point mutation, N448CYH point mutation, K478R-N448CYS double mutation, and K478R-N448CYH double mutation. The results showed that the inhibitors had different binding energies at different positions, with MMRi6 (-7.0 kcal/mol) having the highest docking value in the K478R system, followed by MMRi6 (-6.9 kcal/mol) in the N448CYS system, and the least being MMRi64 (-5.8 kcal/mol) in the N448CYH system. Overall, the average docking scores for the inhibitors suggest that MMRi6 has the highest binding affinity, followed by MMRi64, as shown in **Table 1**.

However, considering the analogous molecules, their difference suggests that MMRi6 may be more sensitive to mutation-induced alterations at the heterodimer interface than MMRi64. The improved docking affinity observed for K478R can be related to the physicochemical properties of arginine. Although lysine and arginine are both basic residues that remain positively charged at physiological pH, substitution of lysine with arginine introduces a guanidinium moiety capable of forming multiple directional hydrogen bonds and highly stable electrostatic interactions. The delocalized positive charge of the guanidinium group allows arginine to participate in more extensive interaction networks than lysine, potentially reshaping the local physicochemical environment of the MDMX RING domain and enhancing ligand accommodation through improved residue–ligand and residue–residue contacts (37,38). These properties have been widely

implicated in the modulation of protein stability, molecular recognition, and allosteric signaling pathways.

Consequently, inhibitors binding within this interface may achieve improved complementarity and stronger intermolecular contacts. Similarly, the N448C mutation appears to influence ligand recognition through modification of local structural stability. Residue N448 resides near the heterodimer interface and has been proposed to contribute to the stabilization of the RING dimer (39,40). Substitution with cysteine, which corresponds to the equivalent residue in MDM2, may promote a more compact interface architecture and reduce unfavorable steric interactions. The improved docking score of MMRi6 in the N448C mutant supports the hypothesis that stabilization of the interface enhances ligand accommodation.

Table 1. Molecular docking results of inhibitors of the wild-type MDM2/X RING protein

	Docking Score (kcal/mol) Ligand	
Systems	MMRi6	MMRi64
WT	-6.5	-6.5
K478R	-7.0	-6.2
N448CYS	-6.9	-6.3
N448CYH	-6.1	-5.8
K478R-N448CYS	-6.6	-6.3
K478R-N448CYH	-5.9	-6.5

3.2 Binding Free Energy (BFE) of MDM2/X RING complexes

To further investigate the effects of mutations at the binding interface between the MDMX and MDM2 RING domains, the MM/GB(PB)SA method was used to calculate binding energy/affinity and interactions. The averaged MD structures of the WT and mutants MDMX RING interface,

interfaced with MDM2 RING, distinctively interacted with inhibitors MMRi6 and MMRi64, constituting the MDMX-binding surface of the protein and MDM2-MDMX RING heterodimeric site. The MM/GB(PB)SA protocol calculates the sum of intermolecular interactions to provide estimates of binding free energy (BFE, ΔGbind), formulated as the sum of gas-phase interaction energy, solvation free energy, and entropy. The calculation was used to predict and correlate induced mutation-induced perturbations in the MDMX-binding surfaces of MDM2-MDMX RINGs (N448C and K478R) mutants and their respective electropositive residues with loss of MDM2-binding affinity. Binding free energy calculations provide a more realistic assessment of protein–ligand affinity than molecular docking because they incorporate conformational sampling from molecular dynamics trajectories and account for solvent-mediated effects that influence ligand stabilization (41).

The total BFE (kcal/mol) for each system was calculated and reported in **Tables 2 and 3**. The result implied that the MMRi6-bound K478R MDMX RING to MDM2 domain exhibited the lowest binding affinity, while the MMRi64-bound single-bound mutant (K478R) and MMRi6-bound double-bound mutant (K478R-N448C) showed the highest binding affinities, with no significant difference. Specifically, the order of increasing binding free energy is K478R-MMRi6 < K478R-N448C-MMRi64 < N448C-MMRi64 < WT-MMRi6 < N448C-MMRi6 < WT-MMRi64 < K478R-N448C-MMRi6 < K478R-MMRi64. The present study demonstrates that mutations within the MDMX RING domain substantially influence the thermodynamic landscape of MMRi6 and MMRi64 binding to the MDM2–MDMX heterodimer. This observation is particularly important because the biological activity of the MDM2–MDMX complex depends on precise RING-domain-mediated heterodimerization, which facilitates E2 recruitment, ubiquitin transfer, and ultimately p53 degradation (42). Structural studies have established that the MDM2–MDMX

RING heterodimer functions as an integrated regulatory unit in which perturbations within either partner can influence the catalytic behavior of the complex (36,39).

For the MMRi6-bound systems, the double mutant K478R/N448C exhibited the most favorable binding free energy (ΔG_bind = –30.05 kcal/mol), followed by N448C (–26.48 kcal/mol), WT (–24.93 kcal/mol), and K478R (–13.26 kcal/mol) (Table 2). These findings indicate that although K478R improved the initial docking affinity of MMRi6, the mutation alone does not provide the most thermodynamically favorable environment for ligand stabilization. Instead, the combined presence of K478R and N448C appears to generate a synergistic effect that enhances long-range intermolecular interactions and promotes a more favorable energetic state for inhibitor retention. This distinction between docking affinity and MMGBSA binding free energy is mechanistically important. Docking evaluates ligand recognition using a largely static receptor conformation, whereas MMGBSA reflects the cumulative energetic consequences of conformational fluctuations occurring throughout the molecular dynamics trajectory. It is therefore common for ligands exhibiting favorable docking scores to display weaker dynamic binding energies if the complex undergoes substantial structural rearrangements after binding (43). The comparatively weak MMGBSA affinity observed for K478R-MMRi6, despite its favorable docking score, suggests that the mutation facilitates ligand accommodation but does not sufficiently stabilize the resulting complex over time. The superior affinity observed for the K478R/N448C-MMRi6 complex appears to arise primarily from favorable gas-phase interactions (-51.53 kcal/mol). In particular, the highly negative van der Waals (-37.12 kcal/mol) and electrostatic energy (-14.41 kcal/mol) contributions indicate that the mutations collectively reorganize the heterodimer interface to maximize attractive intermolecular contacts. This observation is consistent with the structural architecture of the MDM2–MDMX RING heterodimer, where subtle conformational alterations

can propagate through the interface and influence functional communication between the two proteins. Because the RING domains form an extensive interaction surface required for ubiquitination activity, mutation-induced rearrangements that strengthen inhibitor interactions may simultaneously compromise the structural requirements necessary for productive E3 ligase function (42,44,45).

Interestingly, a different energetic pattern emerged for MMRi64. In contrast to MMRi6, the strongest binding free energy was observed for K478R (–30.10 kcal/mol), followed by WT (–27.16 kcal/mol), N448C (–19.94 kcal/mol), and K478R/N448C (–17.72 kcal/mol) (Table 3). These results suggest that MMRi64 responds differently to mutation-induced structural remodeling than MMRi6. Whereas MMRi6 appears to benefit from cooperative effects generated by both mutations, MMRi64 appears to exploit structural changes associated specifically with K478R. One possible explanation for this behavior is that K478R modifies the electrostatic environment around the RING interface in a manner that complements the physicochemical properties of MMRi64. Arginine possesses a guanidinium group capable of forming stronger electrostatic interactions and more persistent hydrogen-bonding networks than lysine (37,38). Consequently, substitution of Lys478 with arginine may increase the persistence of charge-assisted interactions that stabilize MMRi64 throughout the simulation trajectory. The electrostatic contribution observed for K478R-MMRi64 (-8.01 kcal/mol) supports this interpretation, suggesting that mutation-induced redistribution of charge networks contributes substantially to inhibitor recognition. More importantly, the enhanced binding behavior observed for K478R–MMRi64 can be largely attributed to favorable van der Waals interactions (-37.86 kcal/mol) coupled with a beneficial solvent-accessible surface area (E_{SA}) contribution (-4.27 kcal/mol), which are both stronger than those of other complexes (Table 3). The strong van der Waals term suggests improved hydrophobic

packing and closer ligand accommodation within the remodeled binding environment created by the K478R mutation, while the favorable E_{SA} term indicates effective burial of solvent-exposed surfaces upon complex formation. Together, these effects reduce the energetic penalty associated with desolvation and stabilize the protein–ligand complex, thereby contributing substantially to the more favorable binding free energy observed for K478R–MMRi64 (46–48). Notably, all systems exhibited unfavorable positive solvation energies, reflecting the energetic penalty associated with desolvation of the binding interface. However, this penalty was consistently offset by substantially larger favorable van der Waals and electrostatic interactions. Such behavior is characteristic of stable protein–ligand complexes, indicating that inhibitor binding is primarily driven by direct intermolecular interactions rather than solvent-mediated effects (46,49,50).

From a mechanistic perspective, the MMGBSA results support the hypothesis that mutations within the MDMX RING domain can indirectly influence MDM2 structural behavior through allosteric communication across the heterodimer interface. Linke et al. demonstrated that residues located within and around the MDMX RING domain are critical for maintaining the architecture required for productive ubiquitination (51). Consequently, perturbations introduced by K478R and N448C may alter conformational networks that regulate MDM2 function, thereby increasing susceptibility to inhibitor-mediated disruption. These findings pose significant biological implications. The MDM2–MDMX complex negatively regulates p53 through ubiquitination-dependent degradation (42). Therefore, inhibitor-induced destabilization of the functional heterodimer could impair p53 suppression and facilitate restoration of p53-dependent cell-cycle arrest and apoptotic pathways (52). The strong binding free energies observed for K478R/N448C-MMRi6 and K478R-MMRi64 suggest that these mutant systems may experience greater

disruption of the conformational architecture necessary for ubiquitin transfer, thereby enhancing inhibitor efficacy.

Table 2. Thermodynamics analysis: summary of the MM/GBSA-based binding free energy involving MDM2-MDMX (mutated and WT) bound with MMRi6.

	Energy Components (kcal mol^{-1})						
COMPLEX	**ΔE_{VDW}**	**ΔE_{ELEC}**	**ΔG_{GAS}**	**E_{GB}**	**E_{SA}**	**ΔG_{SOLV}**	**ΔG_{BIND}**
WT-MMRi6	-33.33	-7.14	-40.48	19.37	-3.82	15.55	-24.93
	(±3.97)	(±4.93)	(±6.94)	(±4.27)	(±0.43)	(±4.03)	(±4.03)
K478R-MMRi6	-17.77	-17.31	-35.08	24.02	-2.19	21.83	-13.26
	(±7.68)	(11.79)	(±18.16)	(±13.37)	(±0.94)	(±12.56)	(±6.24)
N448C-MMRi6	-33.11	-11.51	-44.62	22.36	-4.23	18.14	-26.48
	(±3.82)	(±6.21)	(±6.98)	(±5.65)	(±0.37)	(±5.56)	(±3.71)
K478R-N448C-	-37.12	-14.41	-51.53	25.59	-4.11	21.48	-30.05
MMRi6	(±3.60)	(±9.70)	(±6.14)	(±0.23)	(±6.12)	(±4.23)	(±7.08)

$\Delta E_{elecidn}$ (electrostatic), ΔE_{vdw} (van der Waals), ΔG_{bind} (calculated total free binding energy), ΔG_{gas} (gas-phase energy), and ΔG_{solv} (solvation free energy).

Table 3. Thermodynamics analysis: summary of the MM/GBSA-based binding free energy involving MDM2-MDMX (mutated and WT) bound with MMRi64.

	Energy Components (kcal mol^{-1})						
COMPLEX	**ΔE_{VDW}**	**ΔE_{ELEC}**	**ΔG_{GAS}**	**E_{GB}**	**E_{SA}**	**ΔG_{SOLV}**	**ΔG_{BIND}**
WT-MMRi64	-35.36	-7.93	-43.28	20.25	-4.13	16.12	-27.16
	(±3.09)	(±3.64)	(±4.78)	(±2.84)	(±0.23)	(±2.78)	(±3.29)
K478R-MMRi64	-37.86	-8.01	-45.87	20.04	-4.27	15.77	-30.10

	(±2.75)	(5.11)	(±5.98)	(±4.38)	(±0.33)	(±4.40)	(±2.92)
N448C-MMRi64	-24.82	-21.08	-45.90	28.89	-2.93	25.96	-19.94
	(±5.30)	(±9.73)	(±13.63)	(±8.61)	(±0.52)	(±8.25)	(±6.28)
K478R-N448C-	-24.35	-22.23	-46.58	31.95	-3.09	28.87	-17.72
MMRi64	(±3.47)	(±9.32)	(±9.13)	(±8.67)	(±0.37)	(±8.67)	(±3.19)

ΔE_{elec} (electrostatic), ΔE_{vdw} (van der Waals), ΔG_{bind} (calculated total free binding energy), ΔG_{gas} (gas-phase energy), and ΔG_{solv} (solvation free energy).

3.3 *Interaction network and per-residue energy contributions*

Per-residue energy decomposition (PRED) is a reliable drug design approach for obtaining residue decomposition rates in protein systems (32). While MMGBSA binding free energy calculations provide a quantitative measure of overall ligand affinity, they do not identify the specific residues responsible for stabilizing protein–ligand complexes. Per-residue energy decomposition, therefore, serves as a valuable complementary approach because it resolves the energetic contributions of individual amino acid residues and enables identification of interaction hotspots that govern inhibitor binding (53). Residue BFE decomposition analysis was carried out across different systems using the MM/GBSA approach to determine their interaction profiles. **Figure 4-11** illustrates the interaction networks, van der Waals (vdW), electrostatic, and total energy contributions of the MMRi6 and MMRi64 systems. In the present study, residue decomposition analysis revealed that mutations within the MDMX RING domain substantially altered the energetic architecture of the MDM2–MDMX heterodimer and redistributed the molecular determinants responsible for stabilizing MMRi6 and MMRi64.The per-residue decomposition energies of all the systems range from -5.4 to 0.9 kcal/mol. Among the MMRi6 systems (**Figure 4-7**), LYS469 in N448C (**Figure 6**) contributed the largest positive electrostatic energy (+0.832

kcal/mol), indicating that the complex might be unstable, while ARG465 has the highest electrostatic energy (-3.435 kcal/mol) in the K478R system (Figure 5). However, PRO444 in the double mutation system also contributed the highest total energy of -3.384 kcal/mol, while ARG465 in the N448C system (**Figure 6**) contributed the highest van der Waals energy (-2.196 kcal/mol).

For the MMRi64 systems (**Figure 8-11**), ARG465 in N448C (**Figure 10**) contributed the most electrostatic energy at -4.767 kcal/mol, while the PRO444 residues in the K478R (**Figure 9**) system contributed the highest total energy at -3.861 kcal/mol, followed closely by WT (**Figure 8**) at -3.804 kcal/mol. On the other hand, ARG465 in the double mutation system has the highest van der Waals energy contribution (-3.353 kcal/mol). A detailed analysis of each complex and its residue decomposition is explained below.

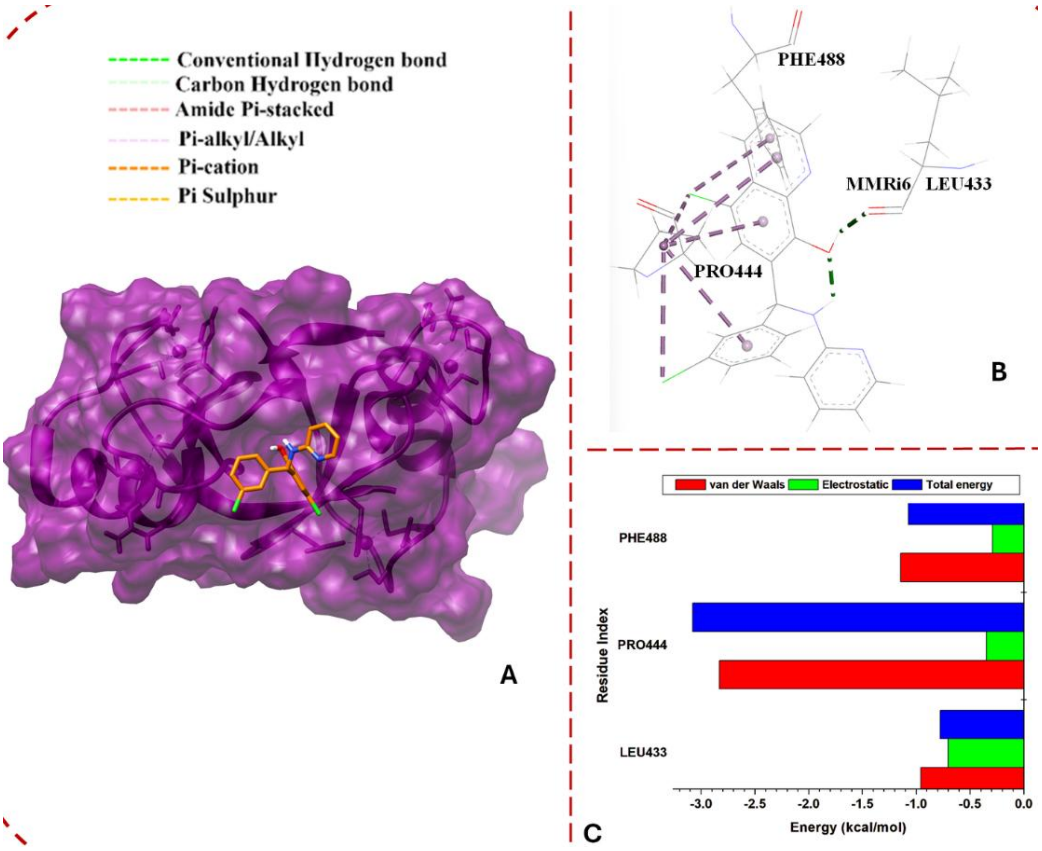


Figure 4. Surface visuals of MMRi6 (orange) complexed with WT MDM2/X (purple) (A). (B) Visual 2D interaction network. (C) per-residue energy contributions.

The PRED analysis for the MMRi6-bound WT system shows that all the residues are located on the MDMX chain. PHE488, one of the active sites of the MDMX chain, has a total energy contribution of -1.070 kcal/mol, vdW of -1.145 kcal/mol, and the lowest electrostatic contribution of -0.293 kcal/mol out of all the residues. PRO444, the residue involved in ligand binding, has the highest total energy contribution and vdW of -3.076 kcal/mol and -2.831 kcal/mol, respectively. LEU433, located at the RING domain interface, has a total energy contribution of -0.777 kcal/mol, vdW of -0.955 kcal/mol, and the highest electrostatic contribution of all the residues (-0.701 kcal/mol). The predominance of hydrophobic residues among the major contributors indicates that stabilization of MMRi6 in the wild-type system is driven primarily by van der Waals interactions rather than electrostatic contacts. This observation is consistent with structural studies demonstrating that hydrophobic packing plays a fundamental role in maintaining the integrity of RING-domain interfaces and contributes significantly to protein-protein recognition events (51). The substantial energetic contribution of PRO444 may reflect the structural role of proline as a conformational anchor within the binding interface. Unlike most amino acids, the cyclic structure of proline restricts backbone mobility and favors well-defined local conformations, thereby helping to preserve the geometric arrangement of neighboring residues involved in ligand recognition. Such rigidity can enhance binding stability by maintaining favorable interaction patterns and reducing conformational fluctuations at the protein–ligand interface (54,55). Consequently, persistent interactions involving PRO444 likely contribute substantially to the favorable binding free energy observed in the WT-MMRi6 system.

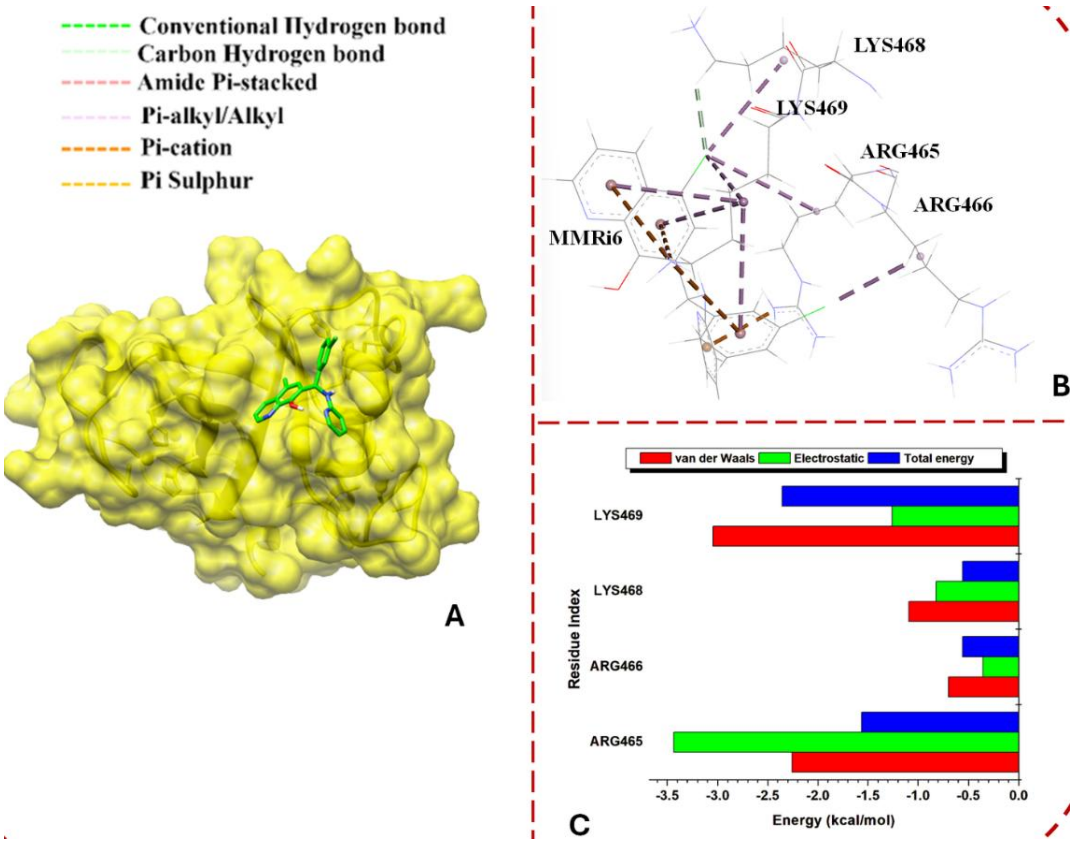


Figure 5. Surface visuals of MMRi6 (green) complexed with MDM2/X (K478R mutation) (yellow) (A). (B) Visual 2D interaction network. (C) per-residue energy contributions.

For the MMRi6-K478R system, all the residues are located on the MDMX chain and form part of the α-helix. A markedly different interaction profile emerged following the introduction of the K478R mutation. Unlike the wild-type system, where hydrophobic residues dominated binding stabilization, the K478R mutant exhibited enhanced participation of charged residues, particularly ARG465 and LYS469. Out of all the residues, ARG465 has the highest electrostatic potential of -3.435 kcal/mol, followed by LYS469 (-1.260 kcal/mol), LYS468 (-0.820 kcal/mol), and then ARG466 (-0.357 kcal/mol). For the total energy contributions, LYS469 has the highest contribution of -2.355 kcal/mol, followed by ARG465 (-1.564 kcal/mol), LYS468 (-0.558 kcal/mol), and finally ARG466 (-0.557 kcal/mol). The vdW contributions in decreasing order are:

LYS469 (-3.046 kcal/mol), ARG465 (-2.256 kcal/mol), LYS468 (-1.092 kcal/mol), and ARG466 (-0.695 kcal/mol). This shift toward electrostatic stabilization is mechanistically significant because substitution of lysine with arginine introduces a guanidinium group capable of forming stronger and more persistent charge-assisted interactions than the primary amine group of lysine. Arginine-mediated interaction networks frequently serve as critical stabilizing elements in protein interfaces owing to their ability to participate simultaneously in multiple hydrogen bonds and electrostatic contacts (37). The emergence of ARG465 and LYS469 as dominant hotspots, therefore, suggests that K478R reorganizes the local electrostatic environment of the MDMX RING domain and redirects ligand stabilization toward charge-driven interactions.

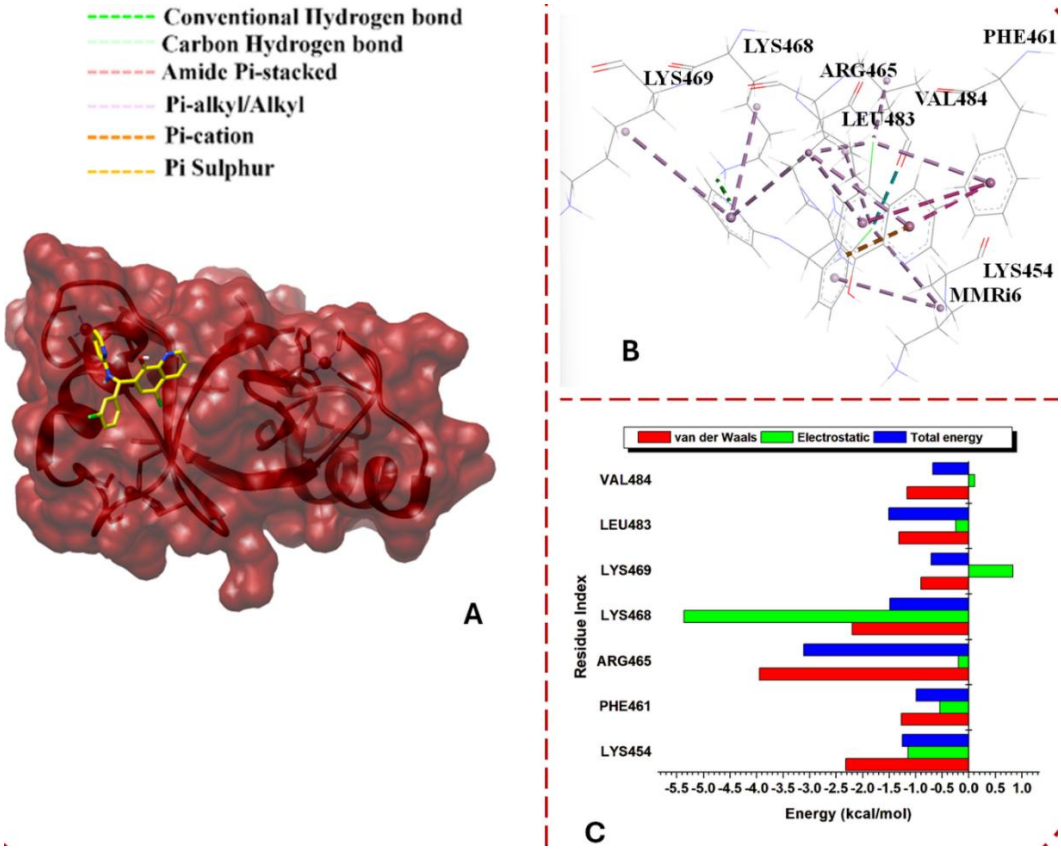


Figure 6. Surface visuals of MMRi6 (yellow) complexed with MDM2/X (N448C mutation) (red) (A). (B) Visual 2D interaction network. (C) per-residue energy contributions.

For the MMRi6-N448C system, LYS454 is the only residue in the loop of the anti-parallel β-sheet on the MDM2 chain, while the other residues are located on the MDMX chain. None of the residues are located at the active sites or ligand-binding sites of the MDM2/X complex. PHE461, ARG465, LYS468, and LYS469 are located on the α-helix of the MDMX chain, while LEU483 and VAL484 are located on one of the β-sheets. LYS469 and VAL484 have positive electrostatic contributions of +0.832 kcal/mol and +0.115 kcal/mol, respectively. LYS468 has the highest electrostatic contribution of -5.359 kcal/mol, followed by LYS454 (-1.143 kcal/mol), PHE461 (-0.541 kcal/mol), LEU483 (-0.244 kcal/mol), and ARG465 (-0.192 kcal/mol).

ARG465 has the highest vdW contribution of -3.942 kcal/mol, followed by LYS454 (-2.316 kcal/mol), LYS468 (-2.196 kcal/mol), LEU483 (-1.312 kcal/mol), PHE461 (-1.272 kcal/mol), VAL484 (-1.159 kcal/mol), and LYS469 (-0.898 kcal/mol). The total energy contributions in decreasing order are: ARG465 (-3.107 kcal/mol), LEU483 (-1.507 kcal/mol), LYS468 (-1.488 kcal/mol), LYS454 (-1.252 kcal/mol), PHE461 (-0.987 kcal/mol), LYS469 (-0.705 kcal/mol), and VAL484 (-0.675 kcal/mol). Similar to K478R, ARG465 remained the dominant contributor, exhibiting the most favorable total energy contribution. However, unlike K478R, the N448C system also recruited additional stabilizing residues, including LYS468 and LEU483. The involvement of multiple residues distributed across the interface suggests formation of a more extensive interaction network capable of stabilizing ligand binding through cooperative effects. Such energetic distribution is frequently associated with enhanced binding robustness because the interaction energy is not dependent upon a single residue or contact point (56,57). This may explain why the N448C mutant displayed substantially more favorable binding free energy than K478R despite sharing several key energetic hotspots.

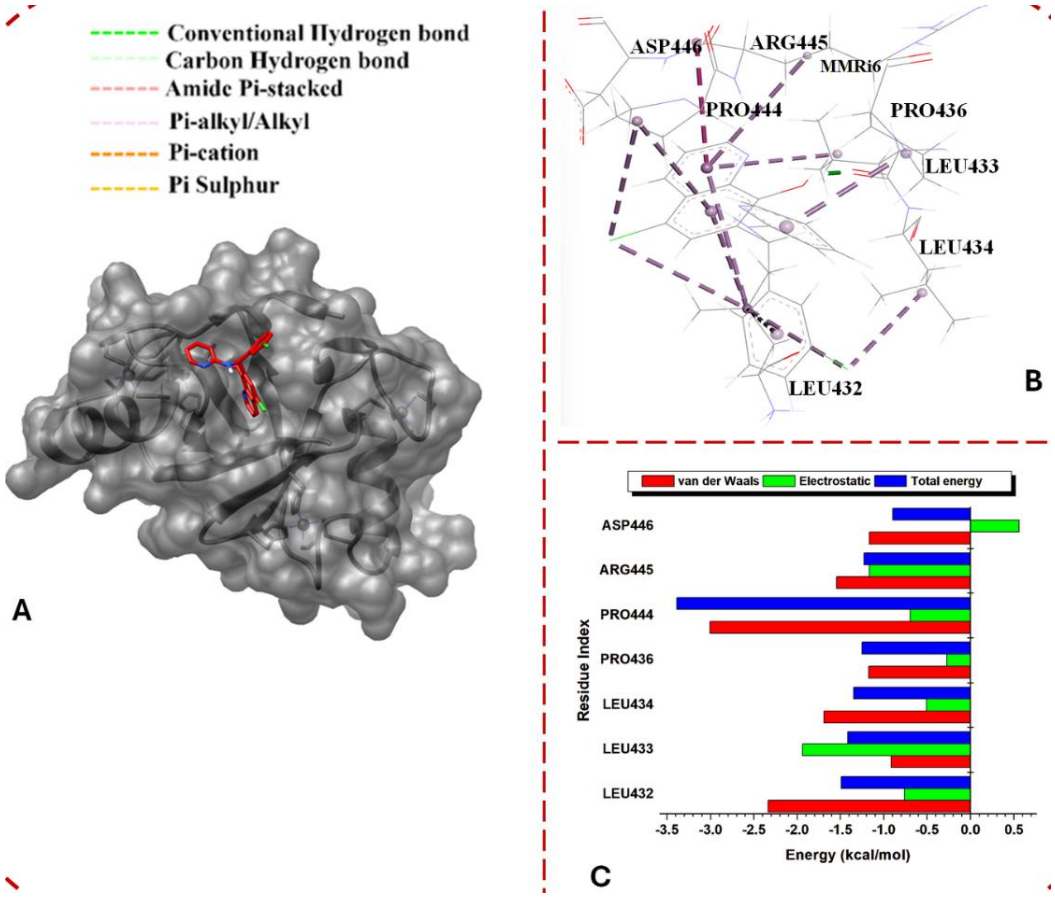


Figure 7. Surface visuals of MMRi6 (red) complexed with MDM2/X (K478R/N448C mutation) (grey) (A). (B) Visual 2D interaction network. (C) per-residue energy contributions.

The most compelling findings were observed in the K478R/N448C double mutant bound to MMRi6. This system exhibited the strongest binding free energy and a distinctive energetic landscape dominated by PRO444, LEU432, LEU433, LEU434, and ILE489. For the MMRi6-K478R/N448C system, LEU432 is the only residue located on the MDM2 chain, while the others are located on the MDMX chain. None of the residues are the active sites of the MDM2/X complex, while PRO444 is a ligand-binding residue on the MDMX chain. ASP446 has a positive electrostatic contribution of +0.560 kcal/mol. LEU433 has the highest electrostatic contribution of

-1.937 kcal/mol, followed by ARG445 (-1.164 kcal/mol), LEU432 (-0.759 kcal/mol), PRO444 (-0.696 kcal/mol), LEU434 (-0.506 kcal/mol), and then PRO436 (-0.270 kcal/mol).

PRO444 has the highest vdW contribution of -3.008 kcal/mol, followed by LEU432 (-2.334 kcal/mol), LEU434 (-1.690 kcal/mol), ARG445 (-1.544 kcal/mol), PRO436 (-1.175 kcal/mol), ASP446 (-1.166 kcal/mol), and LEU433 (-0.913 kcal/mol). The total energy contributions in decreasing order are: PRO444 (-3.384 kcal/mol), LEU432 (-1.491 kcal/mol), LEU433 (-1.418 kcal/mol), LEU434 (-1.348 kcal/mol), PRO436 (-1.251 kcal/mol), ARG445 (-1.228 kcal/mol), and ASP446 (-0.895 kcal/mol). Notably, the interaction profile shifted away from the electrostatic hotspots observed in the single mutants and instead became concentrated around a cluster of hydrophobic residues located at the heterodimer interface. Such a transition suggests that the combined mutations reorganize the binding site architecture in a manner that promotes extensive hydrophobic packing between the inhibitor and the protein surface. Hydrophobic interactions are often major determinants of binding affinity because they contribute favorably to both enthalpic stabilization and solvent exclusion (58). The clustering of favorable interactions around PRO444 and adjacent leucine residues therefore provides a plausible structural explanation for the highly favorable binding free energy observed for the double-mutant MMRi6 complex.

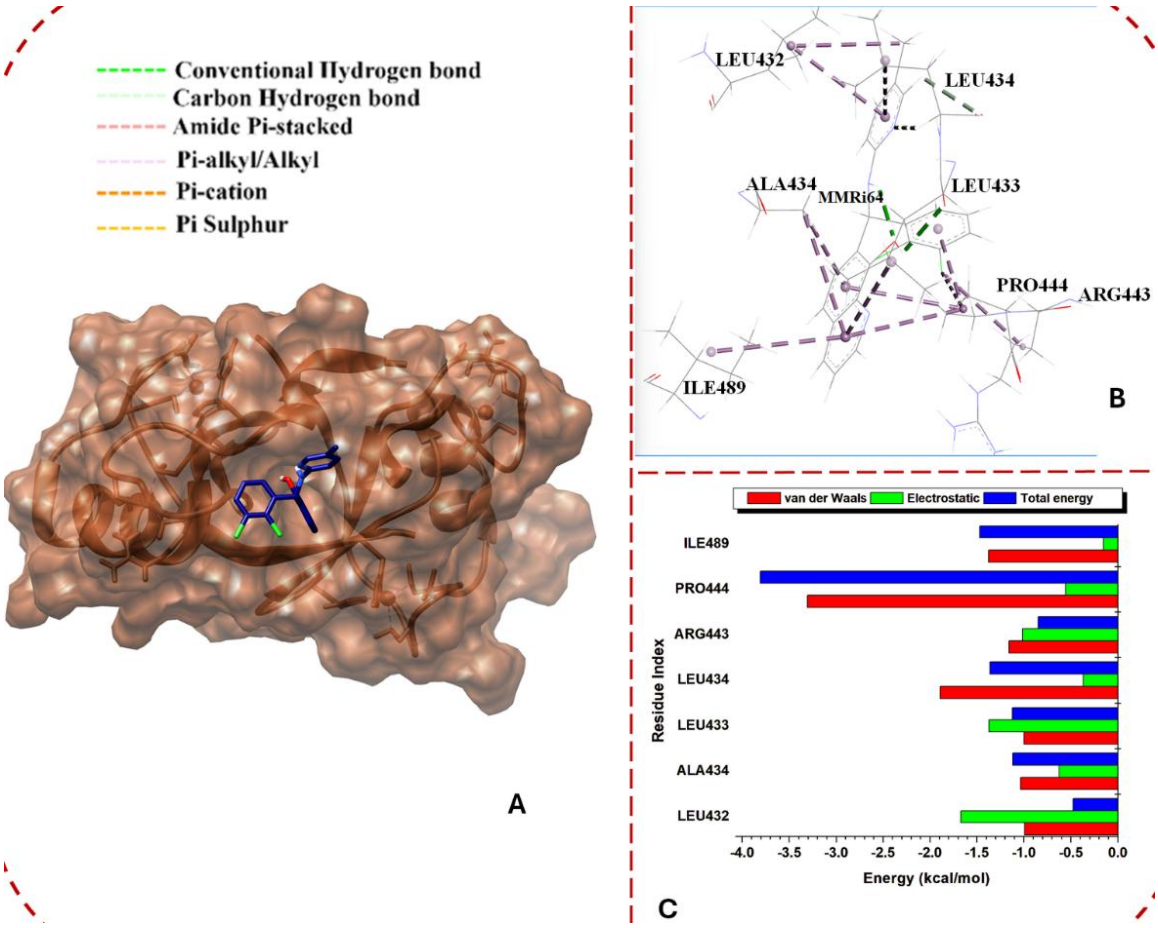


Figure 8. Surface visuals of MMRi64 (blue) complexed with MDM2/X (wild type) (brown) (A). (B) Visual 2D interaction network. (C) per-residue energy contributions.

For this system, LEU432 and ALA434 are located on the MDM2 chain, while the other residues are located on the MDMX chain, with PRO444 being at the ligand-binding site, and ILE489 on a β-sheet. Additionally, ILE489 is an active site residue on the MDMX chain. LEU432 contributes the highest electrostatic energy of -1.672 kcal/mol, followed by LEU433 (-1.369 kcal/mol), ARG443 (-1.013 kcal/mol), ALA434 (-0.625 kcal/mol), PRO444 (-0.555 kcal/mol), LEU434 (-0.368 kcal/mol), and ILE489 (-0.156 kcal/mol).

PRO444 has the highest vdW contribution of -3.306 kcal/mol, followed by LEU434 (-1.892 kcal/mol), ILE489 (-1.374 kcal/mol), ARG443 (-1.155 kcal/mol), ALA434 (-1.032 kcal/mol),

LEU433 (-0.999 kcal/mol), and LEU432 (-0.990 kcal/mol). The total energy contributions in decreasing order are: PRO444 (-3.804 kcal/mol), ILE489 (-1.467 kcal/mol), LEU434 (-1.361 kcal/mol), LEU433 (-1.122 kcal/mol), ALA434 (-1.118 kcal/mol), ARG443 (-0.844 kcal/mol), and LEU432 (-0.476 kcal/mol).

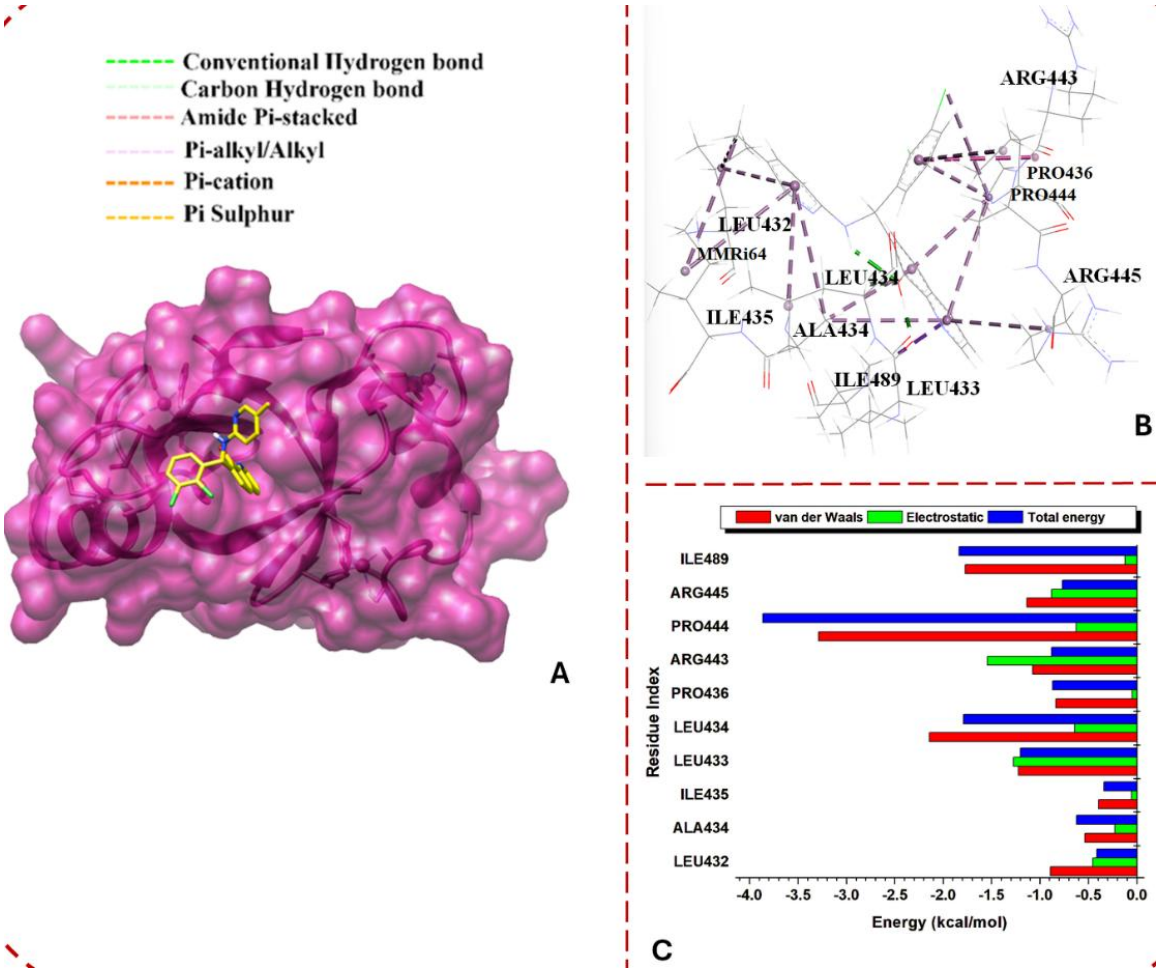


Figure 9. Surface visuals of MMRi64 (yellow) complexed with MDM2/X (K478R mutation) (pink) (A). (B) Visual 2D interaction network. (C) per-residue energy contributions.

In this system, LEU432, ALA434, and ILE435 residues are located on the MDM2 chain, while the other residues are located on the MDMX chain. PRO444 is a residue at the ligand-binding site, and ILE489 is an active site residue on the MDMX chain. The amino acid residue with the highest

electrostatic contribution is ARG443 (-1.541 kcal/mol), followed by LEU433 (-1.273 kcal/mol), ARG445 (-0.878 kcal/mol), LEU434 (-0.640 kcal/mol), PRO444 (-0.623 kcal/mol), LEU432 (-0.457 kcal/mol), ALA434 (-0.226 kcal/mol), ILE489 (-0.122 kcal/mol), ILE435 (-0.056 kcal/mol), and finally PRO436 (-0.048 kcal/mol).

Out of all the residues, PRO444 (-3.289 kcal/mol) contributes the highest vdW energy, followed by LEU434 (-2.143 kcal/mol), ILE489 (-1.771 kcal/mol), LEU433 (-1.221 kcal/mol), ARG445 (-1.133 kcal/mol), ARG443 (-1.074 kcal/mol), LEU432 (-0.891 kcal/mol), PRO436 (-0.834 kcal/mol), ALA434 (-0.539 kcal/mol), and ILE435 (-0.395 kcal/mol). The total energy contributions in decreasing order are: PRO444 (-3.861 kcal/mol), ILE489 (-1.836 kcal/mol), LEU434 (-1.791 kcal/mol), LEU433 (-1.202 kcal/mol), ARG443 (-0.879 kcal/mol), PRO436 (-0.869 kcal/mol), ARG445 (-0.768 kcal/mol), ALA434 (-0.620 kcal/mol), LEU432 (-0.415 kcal/mol), and ILE435 (-0.339 kcal/mol).

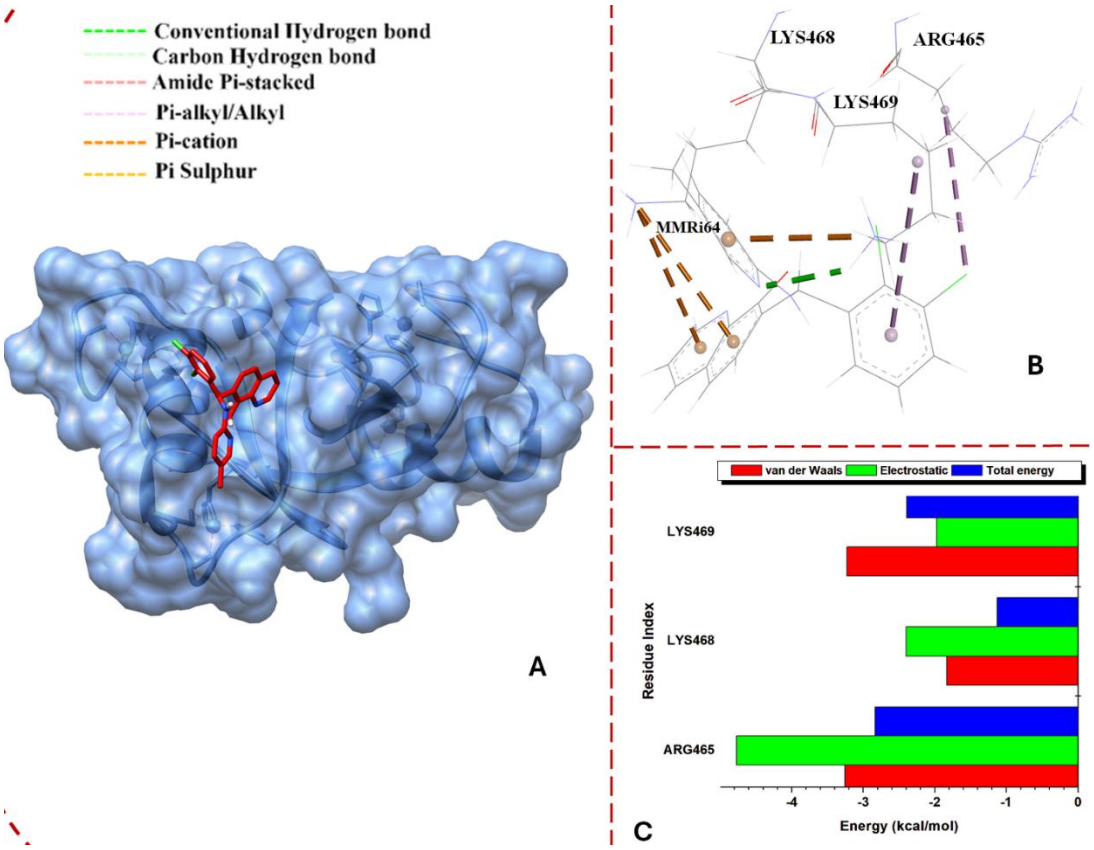


Figure 10. Surface visuals of MMRi64 (red) complexed with MDM2/X (N448C mutation) (blue) (A). (B) Visual 2D interaction network. (C) per-residue energy contributions.

In this system, all the interacting amino acid residues are located on the α-helix of the MDMX chain. None of the residues is at the active site or the ligand-binding site. The residue with the highest electrostatic contribution, ARG465, has a value of -4.767 kcal/mol, followed by LYS468 (-2.400 kcal/mol) and LYS469 (-1.974 kcal/mol).

ARG465 also has the largest vdW contribution of -3.253 kcal/mol, followed closely by LYS469 (-3.228 kcal/mol) and LYS468 (-1.829 kcal/mol). The total energy contributions in decreasing order are: ARG465 (-2.834 kcal/mol), LYS469 (-2.389 kcal/mol), and LYS468 (-1.126 kcal/mol).

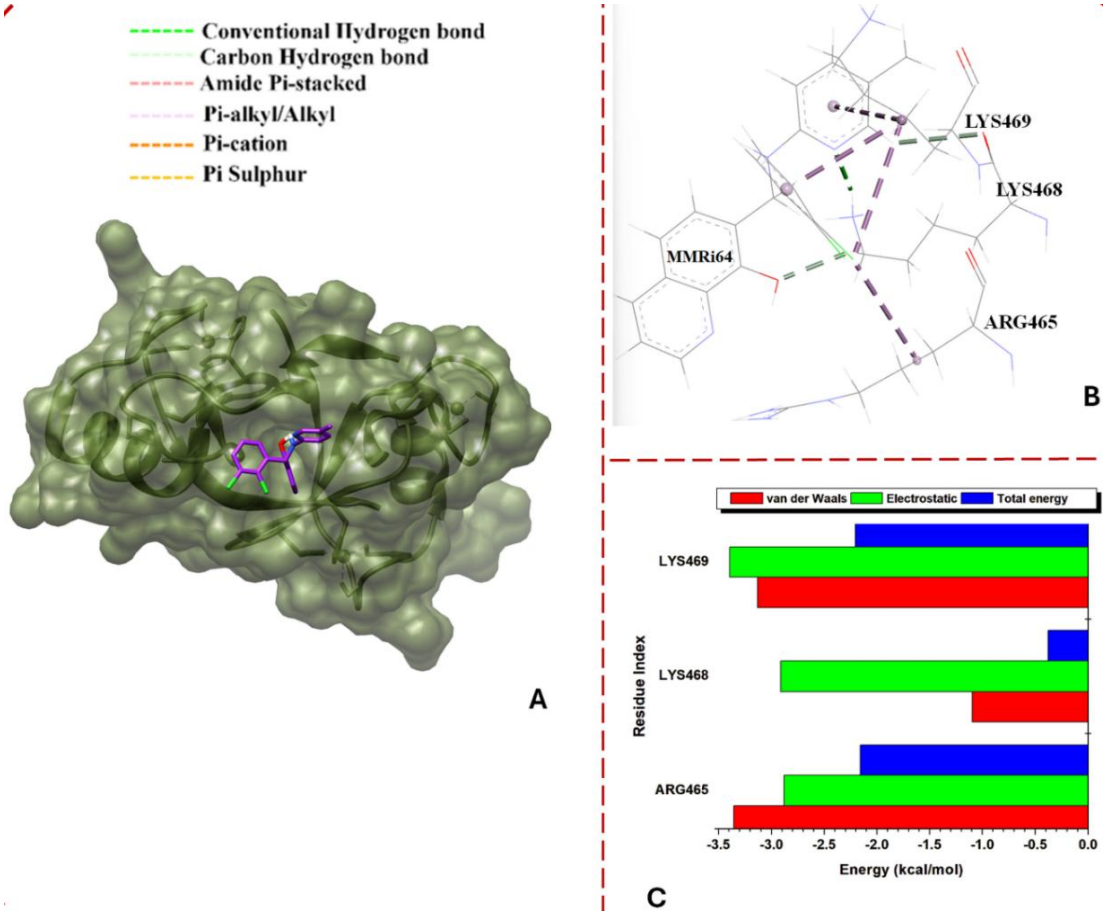


Figure 11. Surface visuals of MMRi64 (purple) complexed with MDM2/X (K478R/N448C mutation) (green) (A). (B) Visual 2D interaction network. (C) per-residue energy contributions.

In this system, all the interacting amino acid residues are located on the α-helix of the MDMX chain. None of the residues is at the active site or the ligand-binding site. LYS469 has the largest electrostatic contribution of -3.393 kcal/mol, followed by LYS468 (-2.911 kcal/mol) and ARG465 (-2.880 kcal/mol). ARG465 has the highest vdW contribution of -3.353 kcal/mol, followed closely by LYS469 (-3.131 kcal/mol) and LYS468 (-1.095 kcal/mol). The total energy contributions in decreasing order are: LYS469 (-2.203 kcal/mol), ARG465 (-2.158 kcal/mol), and LYS468 (-0.380 kcal/mol).

An emerging pattern in the analysis of MMRi64-bound systems shows that, in both WT-MMRi64 and K478R-MMRi64 complexes, PRO444 remained the dominant energetic hotspot, contributing substantially to overall binding stabilization. The persistence of PRO444 across multiple inhibitor classes suggests that this residue functions as a critical interaction node within the MDMX RING domain. Furthermore, the substantial contribution of ILE489 in the K478R-MMRi64 complex implies that the mutation facilitates engagement of residues located closer to functionally important regions of the heterodimer interface. This observation is particularly significant because K478R-MMRi64 exhibited the strongest overall MMGBSA affinity among all MMRi64 systems, indicating that productive engagement of these interface residues may be essential for optimal inhibitor stabilization. In contrast, the N448C-MMRi64 and K478R/N448C-MMRi64 systems displayed energetic profiles dominated by ARG465, LYS468, and LYS469. Although these residues generated highly favorable electrostatic contributions, their overall binding free energies were less favorable than those observed for K478R-MMRi64. This finding further supports the notion that productive inhibitor stabilization requires a balance between electrostatic interactions and hydrophobic packing. Excessive reliance on electrostatic contacts may increase sensitivity to solvent competition and conformational fluctuations, whereas distributed hydrophobic interactions often provide more persistent stabilization over long simulation times (53). The recurring involvement of PRO444, ARG465, LYS468, and LYS469 across multiple systems is particularly noteworthy from a mechanistic perspective. These residues appear to function as central nodes within the interaction network that connects the MDMX RING domain to the broader structural framework of the heterodimer. Given that MDM2–MDMX heterodimerization is required for efficient p53 ubiquitination, perturbation of this interaction center may have consequences extending beyond ligand binding alone. Indeed, previous structural studies have demonstrated that

subtle alterations within the RING interface can substantially influence ubiquitin ligase activity by disrupting conformational communication between MDM2 and MDMX (36,39).

3.4 *System stability, fluctuation, and inter-residual displacement*

The biological activity of the MDM2–MDMX heterodimer depends not only on ligand binding but also on the dynamic structural integrity of the RING domain interface. Since protein function is inherently linked to conformational flexibility, molecular dynamics analyses such as root mean square deviation (RMSD), root mean square fluctuation (RMSF), and principal component analysis (PCA) are particularly valuable for characterizing structural perturbations induced by mutations and inhibitor binding (59–62). Furthermore, structural details into the degree of perturbations and alterations induced across the secondary structures of the WT and mutant MDMX RING (K478R and N448C) could sufficiently reveal the conformational occurrences that impact the heterodimer interface. In the present study, these analyses collectively revealed that K478R and N448C mutations alter the dynamic landscape of the MDM2–MDMX complex and that inhibitor binding amplifies these effects in a mutation-dependent manner.

The root mean square deviation (RMSD), root mean square fluctuation (RMSF), and principal component analysis (PCA) were evaluated in a 200 ns MD simulation for the bound and unbound systems.

The graphical representations of the RMSD, RMSF and PCA plots derived from the C-α atoms are visualised in **Figure 12** below. **Figure 12B** shows that the RMSD plot for the unliganded systems, ApoWT and ApoK478R, is higher than that for the ApoN448C system. These results correlate with their mean values of 4.3 Å and 3.0 Å, respectively, as shown in Table 2.1, indicating that the ApoWT and ApoK478R systems exhibit notable structural differences exceeding 3.0 Å.

Another notable observation from the plot is that the ApoWT becomes stable at around 160 ns, while the ApoK478R system remains unstable throughout the simulation. For the MMRi6 liganded systems, the RMSD table shows that K478R has the highest mean of 2.9 Å, with N448C and the double-mutated K478R/N448C having the same mean of 2.2 Å, and WT having the lowest mean of 2.1 Å. The plot, however, shows that K478R remains relatively stable throughout the simulations, except around 100 ns, when it appears to spike. Apart from this outlier, the MMRi6 systems remained relatively stable throughout the simulations, as their averages remained between 1-3 Å. More importantly, the high mean value of the MMRi6-bound K478R corroborates with the MMRi6 snapshots shown in **Figure 4.2**, showing the obvious alterations that K478R undergoes at the 50-100 ns simulation mark. The fact that RMSD values of the MMRi6-bound complexes remained within the generally accepted range for stable protein systems (1–3 Å) indicates that MMRi6 stabilizes the overall heterodimer architecture regardless of mutational status, while simultaneously permitting localized conformational adaptations required for productive inhibitor engagement. On the other hand, the MMRi64 liganded systems show K478R also having the highest mean value of 4.1 Å, with the lowest being N448C at 1.9 Å. These results indicate that, among all the systems in the RMSD plot, MMRi64-bound N448C exhibits the best stability, and that significant structural differences occur in K478R, as seen in the plot, where the simulation remained mostly unstable until around 135 ns, then became somewhat more stable. This suggests that the K478R mutation significantly enhances the effects of the inhibitors when bound to the MDM2/X complex. These results appear more promising than those of Gunasinghe et al. (2023), who employed inhibitors that bind to MDM2 specifically (63). At first glance, elevated RMSD values are frequently associated with reduced structural stability; such an interpretation may be overly simplistic for inhibitor-bound protein complexes. However, in protein–protein interaction

targets, inhibitors can induce substantial conformational rearrangements that disrupt native communication networks and functional architectures without causing global unfolding. Therefore, increased RMSD may reflect productive conformational reorganization toward inactive or nonfunctional states, a mechanism increasingly recognized as a hallmark of allosteric and PPI-directed inhibition (61,64). This distinction is particularly important for the MDM2–MDMX complex because its ubiquitination activity relies on maintenance of a highly organized RING-domain arrangement (51). Consequently, structural deviations induced by inhibitor binding may represent desirable therapeutic outcomes rather than simple destabilization events. The RMSD findings correlate strongly with the MMGBSA results. Notably, K478R-MMRi64 exhibited both the strongest binding free energy and the largest structural deviation. This relationship suggests that high-affinity binding of MMRi64 does not merely stabilize the protein but actively drives conformational rearrangements throughout the heterodimer. Such behavior is characteristic of allosteric inhibitors, which frequently exert their biological effects by shifting proteins toward alternative conformational states rather than simply occupying a binding pocket (65). The ability of MMRi64 to induce substantial structural changes in the K478R mutant, therefore, provides compelling evidence that mutation-enhanced binding is associated with functional perturbation of the MDM2–MDMX interface.

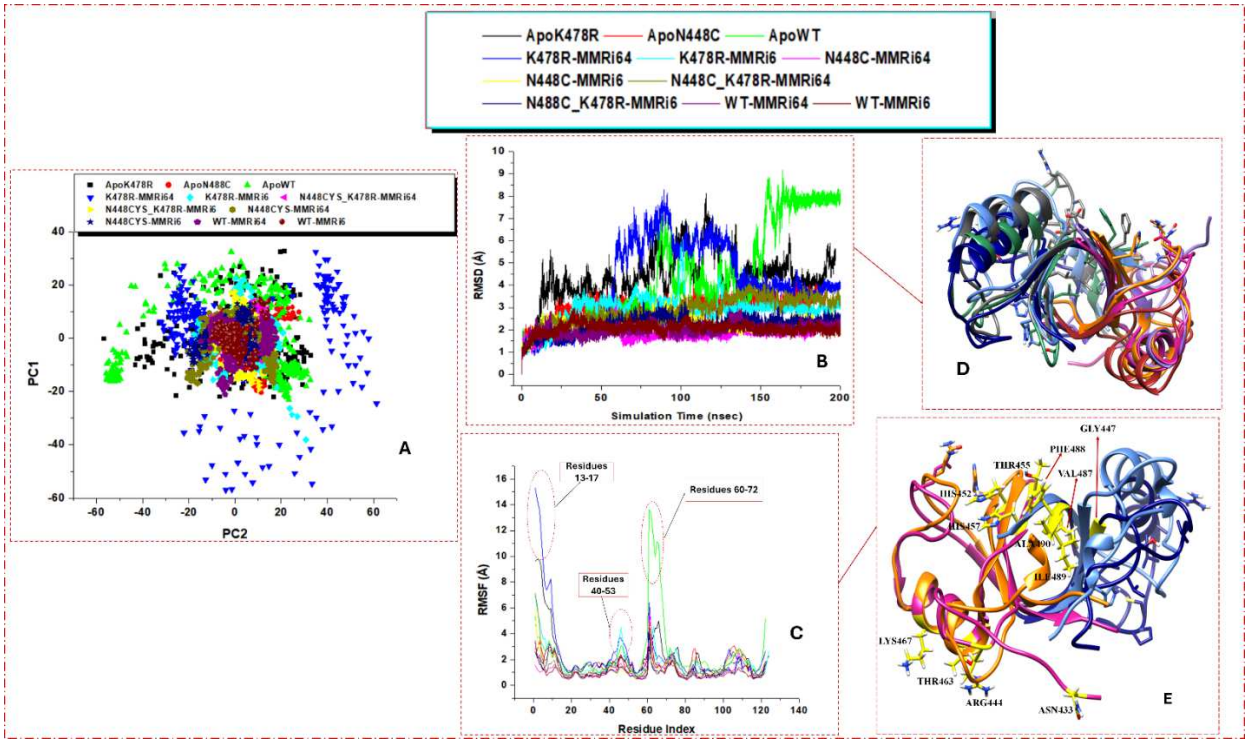


Figure 12. Comparative PCA (A), RMSD (B), and RMSF (C) for the Apo systems (MMRi6-bound and MMRi64-bound). (D) represents superimposed snapshots for ApoWT (1 ns), WT-MMRi6 (150 ns), K478R-MMRi64 (150 ns), and K478R/N448C-MMRi64 (150 ns). (E) shows superimposed ApoWT with double mutation K478R/N448C-MMRi64; the active site residues of the MDM2/X are labelled accordingly. Colour outlines for chains C and D, respectively: ApoWT (orange and cornflower blue), WT-MMRi64 (brown and dim grey), K478R mutated (medium purple and sea green), K478R/N448C double mutation (violet red and navy blue).

To further characterize local flexibility, RMSF analysis was performed. The RMSF plot represented in **Fig. 12C** focuses on the level of flexibility within the different systems. The fluctuations shown in the RMSF plot indicate that for the Apo systems, ApoWT has the highest average value of 2.5 Å, while ApoN448C has the lowest at 1.6 Å. For the MMRi6 systems, K478R has the highest average of 1.7 Å, and WT has the lowest at 1.0 Å. The MMRi64 systems show that K478R has the highest RMSF of 2.5 Å, whereas N448C has the lowest at 1.1 Å. These findings

suggest that the K478R system for both inhibitors exhibits the highest flexibility and mobility, as indicated by the RMSD plot.

Furthermore, ApoWT, which has the greatest mean value out of all the unliganded systems, exhibits the highest fluctuations at residues 60-72 (**Fig. 12C**). This suggests that these residues are made up of loops and are less constrained by internal interactions. Previous studies have demonstrated that loop regions frequently serve as mediators of allosteric communication because their intrinsic flexibility enables transmission of conformational signals between distant functional sites. Consequently, mutation-induced changes in loop mobility can influence protein activity by altering interaction networks, ligand recognition processes, and long-range communication pathways that underpin biological function (66,67). Particularly notable were the fluctuations occurring at residues 13–17 in the MMRi64-K478R system and residues 40–53 in the MMRi6-K478R system. These regions may represent dynamic hotspots through which inhibitor-induced perturbations propagate across the heterodimer interface. Increased mobility within these segments could disrupt the structural communication necessary for coordinated ubiquitin transfer and consequently impair p53 degradation. The least fluctuation seems to occur at the MMRi6-bound WT system, which indicates that it is the most stable system, and its secondary structure is most likely made up mainly of alpha-helices and beta-sheets, which correlate with the DSSP plot in **Fig. 15D**. **Tables 4** and **5** show the mean RMSD and RMSF of the unliganded and ligand-bound MDM2-MDMX RING domain proteins, respectively. Together, these findings suggest that inhibitor efficacy may depend not only on stabilization of ligand binding but also on the extent to which binding perturbs biologically relevant conformational states (61).

Table 4. Showing the mean values of the root mean square deviation (RMSD) and root mean square fluctuation (RMSF) for the unliganded systems. All values are in Angstrom (Å).

System	RMSD	RMSF
ApoWT	4.3 ± 2.149	2.5 ± 2.398
ApoK478R	4.3 ± 1.075	2.2 ± 1.834
ApoN448C	3.0 ± 0.509	1.6 ± 0.765

Table 5. Showing the mean values of the root mean square deviation (RMSD) and root mean square fluctuation (RMSF) for the liganded systems. All values are in Angstrom (Å).

	MMRi6		MMRi64	
System	**RMSD**	**RMSF**	**RMSD**	**RMSF**
WT	2.1 ± 0.243	1.0 ± 0.470	2.0 ± 0.266	1.3 ± 0.693
K478R	2.9 ± 0.644	1.7 ± 1.089	4.1 ± 1.778	2.5 ± 2.614
N448C	2.2 ± 0.316	1.3 ± 0.856	1.9 ± 0.288	1.1 ± 0.707
K478R/N448C	2.2 ± 0.370	1.1 ± 0.611	2.8 ± 0.613	1.5 ± 0.968

Principal component analysis (PCA) is a computational matrix method that projects high-dimensional molecular dynamics data into a lower-dimensional space and was applied to C-α atoms to explore conformational variations between the unliganded and liganded systems.(68) A visual representation of the PCA analysis is shown in **Figure 12A**, where the individual vectors (*ev1* vs *ev2*) are projected onto the PC1 and PC2 components.(32)

The scatter plot shows the displacement of the unliganded and liganded systems, with the C-α of the MMRi64-bound K478R system being most displaced, followed by ApoWT and ApoK478R. From the plot, the most compact system seems to be the MMRi6-bound WT, which aligns with its

RMSD and RMSF having the lowest mean value among the MMRi6-bound systems. The broad conformational distribution observed for K478R-MMRi64 is particularly significant because it suggests that inhibitor binding promotes transitions between multiple structural substates rather than stabilization of a single dominant conformation. Such behavior is frequently associated with allosteric modulation and can reflect disruption of coordinated motions required for protein function (69). Importantly, the PCA findings corroborate both RMSD and RMSF results, providing independent evidence that the K478R mutation enhances the ability of MMRi64 to reshape the conformational landscape of the MDM2–MDMX heterodimer.

3.5 *Compactness/mobility and solvent exposure on MDM2/X surface changes*

The structural integrity of the MDM2–MDMX heterodimer is essential for its ability to coordinate ubiquitin transfer and regulate p53 degradation. Consequently, analyses that quantify global compactness and solvent accessibility provide valuable insight into the structural consequences of mutation and inhibitor binding (51,70). Solvent-accessible surface area (SASA) provides insight into changes in a protein when it is exposed to solvent. This analysis was conducted using the 'surf' command to implement a linear combination of pairwise overlaps (LCPO) algorithm in the AMBER tools 18 GPU CPPTRAJ module.(71) The SASA plot in **Figure 13A** below shows that the ApoWT and MMRi64-bound K478R systems exhibit the greatest fluctuations, with the latter's surface area hovering around 8500 Å, whereas the MMRi6-bound WT and N448C systems remain relatively stable throughout the simulations. This implies that the high-fluctuation systems are unstable in solvent and indicates that the hydration networks at the binding site of the K478R system were displaced upon binding of the MMRi64 inhibitor. **Figure 13C** represents the visualisations of water molecules bound to different sites in the ApoK478R, MMRi64-bound K478R, double mutation, and K478R systems. The common hydration site across all these systems

is GLN480 on Chain C, indicating that this site hosts stable, ordered networks. The only other hydration site on Chain C is located at GLU436 in the MMRi64-bound system. ASP446 is also common to the MMRi64-bound WT and K478R systems, suggesting this residue is only stable in these systems. Other hydration sites located on Chain D include HIS456 (ApoK478R), ARG445 (WT-MMRi64), and THR454 (K478R-MMRi64).

Following the SASA analysis, the apo systems displayed relatively high solvent-accessible surface areas, reflecting exposure of residues at the protein surface and within flexible interface regions. ApoWT exhibited the largest average SASA value, consistent with its elevated RMSD, RMSF, and RoG measurements. In contrast, ApoN448C displayed reduced SASA values, further supporting the conclusion that this mutation promotes a more compact and less solvent-exposed structural state. Upon inhibitor binding, a general reduction in SASA was observed for most systems. Such decreases are commonly associated with burial of hydrophobic residues and formation of tighter intermolecular contacts within protein–ligand complexes (43). Such ligand-induced surface burial is often associated with stabilization of specific conformational states and may contribute to inhibition by restricting the dynamic rearrangements required for productive ubiquitin ligase activity (72). The reduction in solvent exposure observed for MMRi6-bound systems is therefore consistent with the favorable van der Waals interactions identified in the MMGBSA calculations and the hydrophobic interaction networks revealed by residue decomposition analysis. In contrast, K478R-MMRi64 maintained relatively higher SASA values despite possessing the strongest MMGBSA affinity among MMRi64 systems. This result indicates that strong inhibitor binding does not necessarily require maximal burial of solvent-exposed surface area. Rather, the inhibitor may stabilize partially open conformations that remain energetically favorable due to persistent electrostatic and hydrophobic interactions (62). Such

behavior aligns closely with the PCA results, which demonstrated extensive conformational sampling by the K478R-MMRi64 complex. The persistence of solvent exposure in this system may therefore reflect stabilization of alternative conformational states associated with disruption of functional heterodimer organization (39).

Radius of gyration (RoG) analysis was also performed to assess the compactness of the systems in the liganded and unliganded states (63). From the RoG plot in **Fig. 13B**, the ApoWT system has the least stability and compactness, with a mean value of 15.7 Å, as shown in Table 3.1, while the MMRi64-bound K478R/N448C system has the highest mean value of 15.5 Å for the liganded systems (Table 3.2). On the other hand, the MMRi6-bound K478R/N448C system appears to be the most compact, with a mean value of 14.7 Å. This implies that the combination of the double mutation and MMRi64 greatly impacted the stability of the MDM2/X complex. However, a closer look at the MMRi64-bound K478R system shows that it has quite a close RoG value to the MMRi64-bound K478R/N448C system. This seems more promising, as it corroborates the RMSD, RMSF, PCA, and even SASA results. In addition, **Fig. 13D** shows a superimposed visualisation of the ApoWT and MMRi64-bound K478R systems. It shows that while these systems have the highest RoG values, Chain D specifically has the greatest impact because it is not aligned.

The radius of gyration (RoG) analysis revealed distinct mutation-dependent effects of inhibitor binding on the overall compactness of the MDM2–MDMX heterodimer. The radius of gyration analysis revealed notable differences between the apo and ligand-bound systems. Upon MMRi6 binding, all systems showed reduced RoG values relative to their apo counterparts, with the K478R/N448C–MMRi6 complex exhibiting the greatest degree of compaction (14.7 Å). This observation is consistent with the favorable MMGBSA binding free energy reported for the double mutant–MMRi6 complex and suggests that strong ligand binding stabilizes a compact inhibitor-

bound conformation. Such compaction may restrict the conformational flexibility required for proper alignment of the MDM2–MDMX RING domains during E2 enzyme recruitment and ubiquitin transfer, thereby impairing ubiquitination activity (34,36). Thus, the enhanced compactness observed in the double mutant likely reflects successful optimization of the interaction network identified in the residue decomposition analysis. The behavior of MMRi64-bound systems was markedly different. The K478R-MMRi64 complex exhibited larger fluctuations in RoG and sampled a broader range of conformations than the other systems. These expanded conformations correlate closely with the elevated RMSD values and broader conformational sampling observed during PCA analysis for the same systems. Rather than indicating simple structural instability, the concurrent occurrence of strong MMGBSA binding affinity and increased RoG suggests that MMRi64 promotes ligand-stabilized conformational remodeling. Recent studies have shown that effective protein–protein interaction inhibitors frequently function by shifting targets toward alternative conformational ensembles that are energetically favorable yet functionally nonproductive (61). Therefore, the increased RoG observed for K478R–MMRi64 likely reflects disruption of the highly ordered geometric arrangement required for efficient MDM2–MDMX-mediated ubiquitination rather than loss of structural integrity.

Table 6. Showing the mean values of the radius of gyration (RoG) for the unliganded systems. All values are in Angstrom (Å).

System	RoG	SASA
ApoWT	15.7 ± 0.560	7431.14 ± 394.37
ApoK478R	15.6 ± 0.351	7416.11 ± 252.27
ApoN448C	15.2 ± 0.210	7351.93 ± 217.20

Table 7. Showing the mean values of the radius of gyration (RoG) for the liganded systems. All values are in Angstrom (Å).

		MMRi6	MMRi64	
System	**RoG**	**SASA**	**RoG**	**SASA**
WT	14.9 ± 0.167	6543.74 ± 195.98	14.8 ± 0.178	6568.75 ± 200.11
K478R	15.2 ± 0.244	6817.86 ± 239.09	15.4 ± 0.511	7458.98 ± 399.63
N448C	15.1 ± 0.195	6641.87 ± 185.50	15.0 ± 0.174	7130.63 ± 281.15
K478R/N448C	14.7 ± 0.166	6756.85 ± 272.83	15.5 ± 0.295	6440.82 ± 233.19

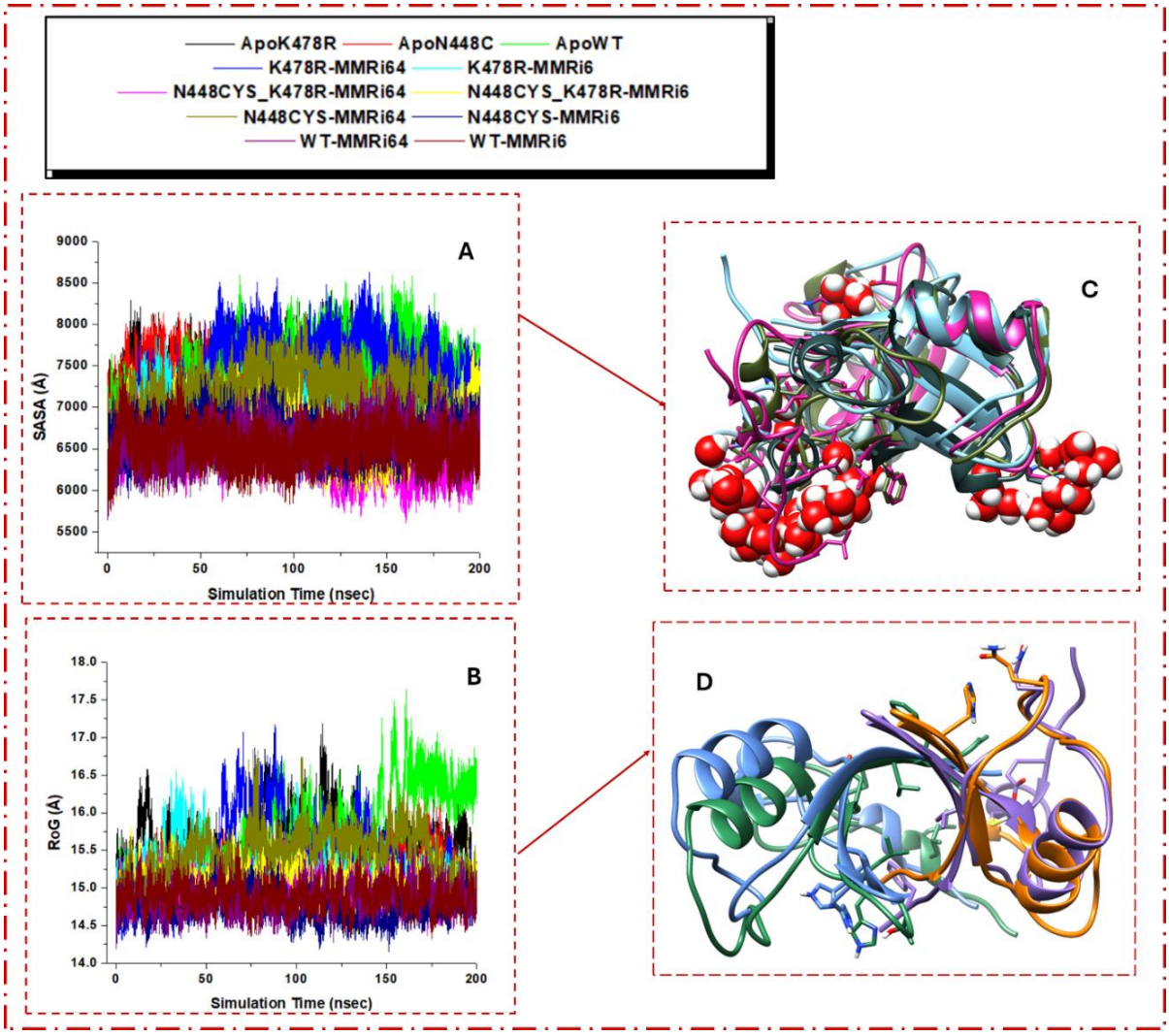


Figure 13. Comparative SASA (A) and ROG (B) for the Apo systems, MMRi6-bound and MMRi64-bound systems. (C) represents superimposed snapshots for ApoK478R (1 ns) (dark slate gray), WT-MMRi64 (150 ns) (dark olive green), K478R-MMRi64 (150 ns) (violet-red), and K478R/N448C-MMRi64 (150 ns) (sky blue); water molecules are represented in spheres. (D) shows superimposed ApoWT with K478R-MMRi64. Colour outlines for chains C and D, respectively: ApoWT (orange and cornflower blue), K478R mutated (medium purple and sea green).

3.6 *Defined secondary structure of mutated MDM2/X RINGs* systems

The Defined Secondary Structure of Proteins (DSSP) analysis is important for characterising secondary structure elements, such as α-helices, β-pleated sheets, and loops, in protein molecules and for tracking structural changes over different simulation times (73). In the context of the MDM2–MDMX heterodimer, DSSP analysis is particularly relevant because the RING domain functions through a highly organized structural framework that must be maintained to facilitate productive E2 enzyme recruitment and ubiquitin transfer (51).

The DSSP analysis for the Apo systems represented in **Fig. 14** shows structural changes between residues 61-71 from alpha helix, bends, and 3-10 in the WT (**Fig. 14A**), to almost no definite structure in the K478R (**Fig. 14B**) and turns and parallel sheets in N448C (**Fig. 14C**). Significant changes from turns to bends also occurred between residues 21-31 from 0-150 ns in **Fig. 14B,** but became turns again at the last 50 ns.

These alterations imply that the K478R and N448C mutations affect the stability of the secondary structures of the MDM2/X complex, even in the absence of ligand binding. Analysis of the apo systems revealed that the wild-type (ApoWT) heterodimer exhibited greater secondary structure fluctuations and conformational mobility than the mutants, consistent with RMSD and RMSF data. This flexibility likely originates from transient secondary structural rearrangements rather than large-scale domain movements. Conversely, the ApoN448C system displayed stable secondary structure profiles with conserved α-helical and β-sheet regions. This aligns with its reduced RMSD, RMSF, SASA, and RoG values, confirming that the Asn448Cys substitution enhances structural stability within the MDMX RING domain, potentially by strengthening interdomain packing at the interface. The K478R mutant showed intermediate behavior; while its global fold remained preserved, localized turn and bend transitions occurred more frequently than in N448C,

matching RMSF and PCA trends. Such localized perturbations can significantly alter protein activity via allosteric communication networks (69).

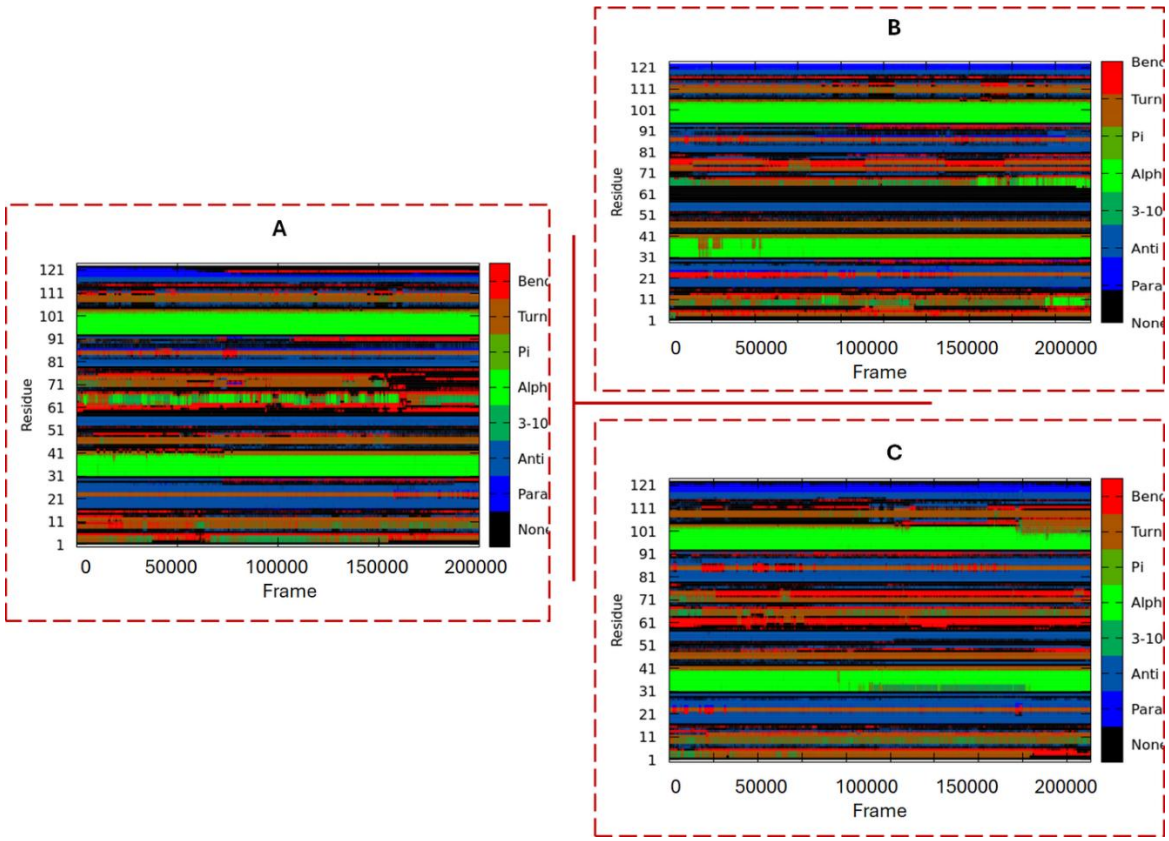


Figure 14 The DSSP systems for unliganded MDM2/X protein systems taken throughout 200 ns MD simulations: (A) ApoWT MDM2/X. (B) ApoK478R mutation. (C) ApoN448C mutation.

For the MMRi6-bound systems, significant alterations occurred in the K478R system (**Fig. 15A**) compared to **Fig. 15D**, where no definite structure was observed throughout the 200 ns simulation between residues 61 and about 68. Residues 41-51 on K478R, N448C and the double mutation systems also show changes from 3-10 helices to turns. Furthermore, residues 1-11 in **Fig. 15C** depict changes from bends to 3-10 helices at the 50-200 ns simulation mark.

Comparing the MMRi6-bound systems to the Apo systems, the secondary structures of residues 1-11 in **Fig. 15B** change to no definite structure between the 100-200 ns simulation mark, unlike the Apo system (**Fig. 14C**), whose residues have a combination of turns, bends and 3-10 helices. This indicates that binding of MMRi6 to the N448C mutant system alters its stability and induces fluctuations in the MDM2/X secondary structures.

Furthermore, the analysis also shows a significant difference in the structures of the ApoWT (**Fig. 14A**) and WT-MMRi6 (**Fig. 15D**), with changes occurring in residues 41-51, 61-71, and 111-121. These differences inevitably indicate that the binding of the MMRi6 ligand significantly affects the secondary structure and stability of the WT system.

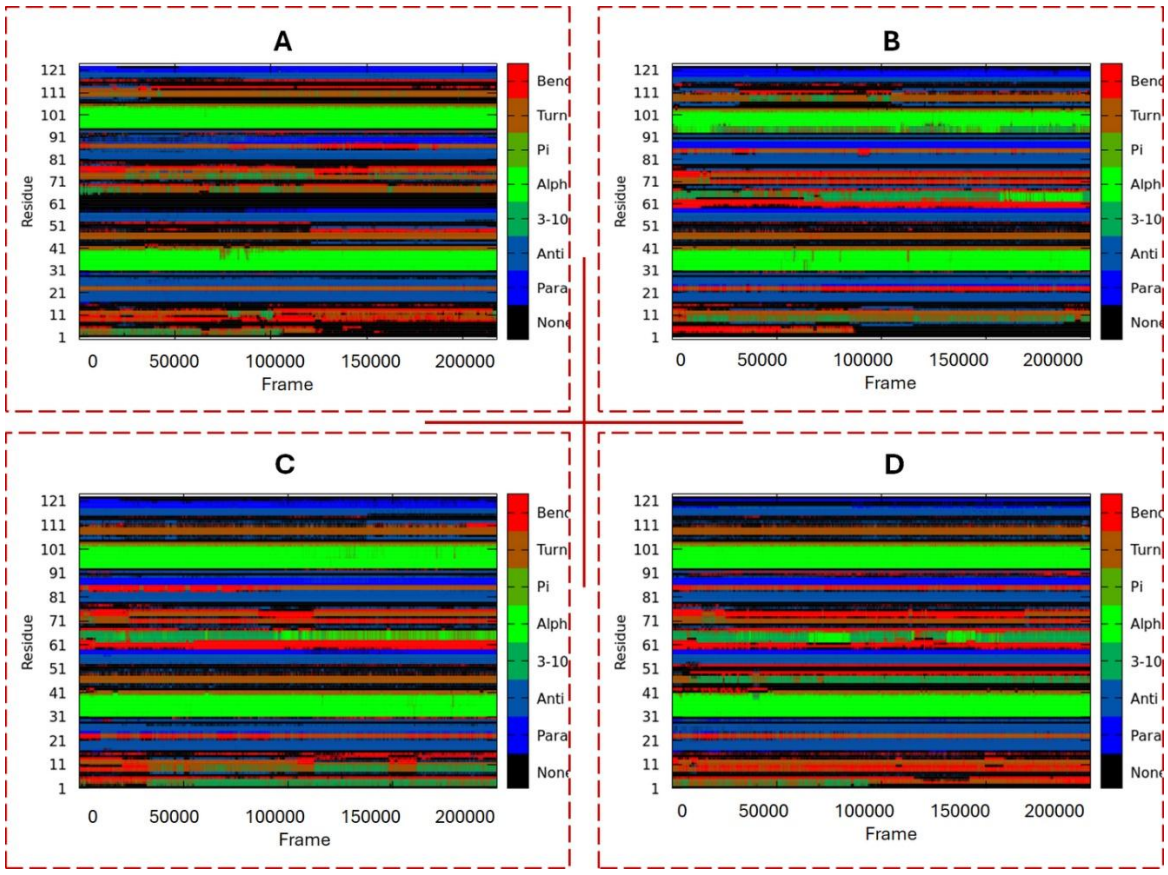


Figure 15. The DSSP systems for liganded MDM2/X protein systems with **MMRi6** taken throughout 200 ns MD simulations: (A) K478R mutation. (B) N448C mutation. (C) K478R/N448C mutations. (D) WT-liganded.

Using the WT-MMRi64 (**Fig. 16D**) as a reference for the other results in **Fig. 16**, significant changes occurred at residues 1-11 for all the other systems, with K478R-MMRi64 (**Fig.16A**) having alpha helices at the 100-200 ns simulation mark, **Fig. 16B** having majorly turns, and **Fig. 16C** having no definite structure at the 100-200 ns simulation mark.

The ApoWT (**Fig. 14A**) and MMRi64-WT (**Fig. 16D**) also show significant differences, with **Figure 16D** almost completely losing its bends between residues 41-51. There are also changes at residues 61-71 and 111-121. In addition, changes also occur between **Fig. 14B** and **Fig. 16A**, particularly at residues 61-71. The MMRi64-bound N448C (**Fig. 16B**) and Apo-N448C (**Fig. 14C**) systems also show significant differences at residues 1-11 and between residues 91-101 at the 175-200 ns simulation mark.

MMRi6 binding generally preserved secondary structural elements across the WT, N448C, and K478R/N448C complexes. These systems displayed stable α-helical and β-sheet content with minor loop fluctuations, aligning with favorable MMGBSA binding free energies and compact conformational ensembles. This thermodynamic stabilization suggests MMRi6 modulates protein dynamics rather than disrupting structural architecture. Notably, the K478R/N448C-MMRi6 complex showed exceptional DSSP stability, consistent with an extensive hydrophobic interaction network and cooperative effects optimizing the inhibitor-bound state without losing secondary structure.

Conversely, the K478R-MMRi64 complex revealed pronounced transitions from ordered turns/bends to disordered coils. Despite exhibiting the strongest MMGBSA binding affinity, this system also showed the highest RMSD and broadest PCA distribution, indicating that strong inhibitor binding drives local structural remodeling and plasticity rather than simple stabilization. This localized coil formation likely disrupts the conformational networks required for interface communication, representing a mechanistic basis for suppressing MDM2–MDMX activity through functional inactivation (42).

Crucially, no mutation or inhibitor induced extensive unfolding over the 200 ns simulations; the heterodimer framework remained intact. This indicates targeted modulation of functional dynamics rather than nonspecific destabilization (61,64,74). The inhibitors appear to exploit specific conformational vulnerabilities within the heterodimer, particularly K478R-MMRi64, exhibited localized secondary structural transitions that may facilitate propagation of allosteric effects across the protein. Overall, the DSSP findings bridge energetics and dynamics: N448C promotes secondary structure stabilization and strengthens interdomain packing, whereas K478R enhances local plasticity and responsiveness to inhibitor binding. Together, these mutations modulate the precise balance between stability and conformational adaptability within the MDMX RING domain.

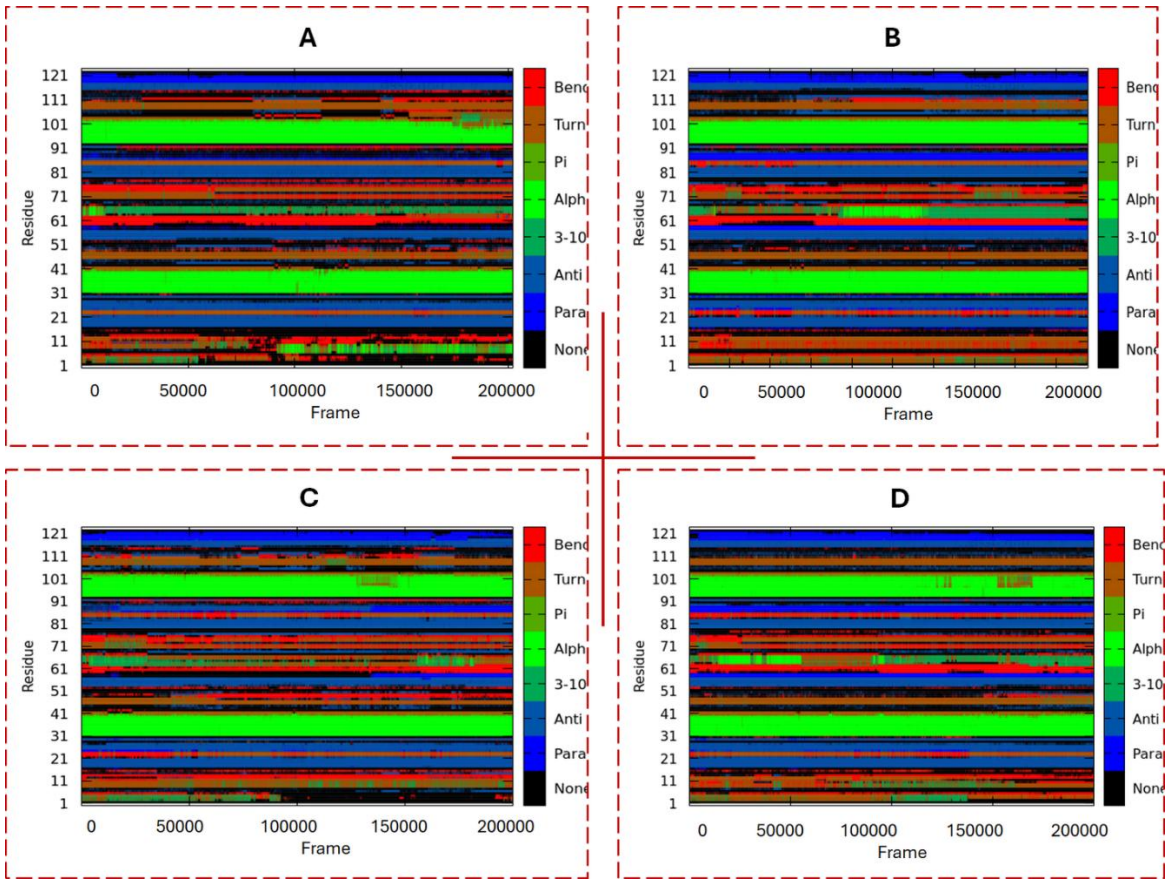


Figure 16. The DSSP systems for liganded MDM2/X protein systems with **MMRi64** taken throughout 200 ns MD simulations: (A) K478R mutation. (B) N448C mutation. (C) K478R/N448C mutations. (D) WT-liganded

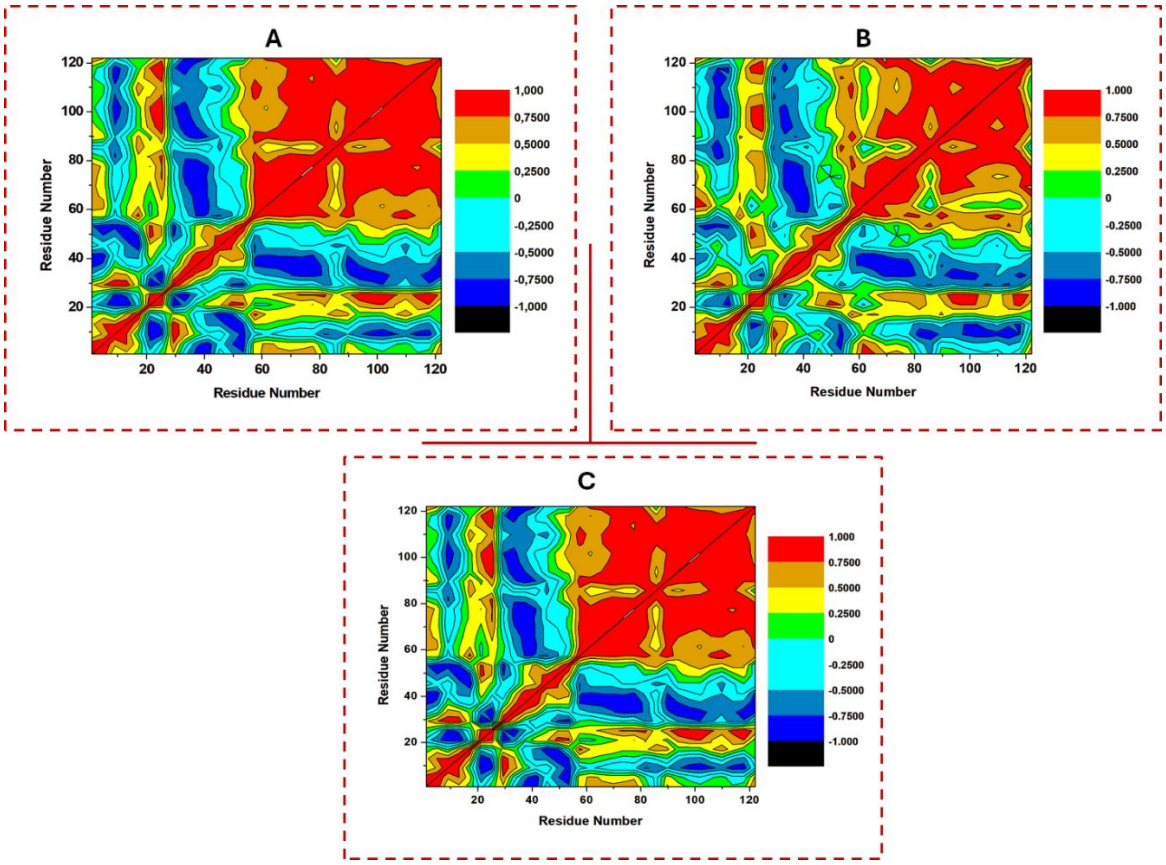
3.7 *Dynamic cross-correlation matrix (DCCM)*

The DCCM was determined during 200 ns MD simulations to reveal structural fluctuations and identify the positions of atoms and their correlated motions in the unliganded and liganded systems. **Figs 17–19** show the correlated motions of C-α atoms across the different systems, indicating positive (red to yellow), negative/anti-correlated (cyan to black), and similar (green) correlation (32,75).

Fig. 17, representing the unliganded systems, indicates that ApoK478R and ApoWT (17A and 17C, respectively) exhibit the highest degree of positively correlated movements, indicating that their C-α atoms move in the same direction and are more stable. These results agreed with the high RMSF average values (**Fig. 12C**). However, **Fig. 17B** shows a reduced positive correlation in the ApoN448C system, with a corresponding lower average RMSF. Among the residues, the systems also exhibit negative correlations, indicating movement in opposite directions and instability.

Figure 17. The dynamic cross-correlation matrix (DCCM) for unliganded MDM2/X protein systems, averaged over 200 ns MD simulations: (A) ApoK478R mutation. (B) ApoN448C mutation. (C). ApoWT MDM2/X.

Fig. 18. Below is a representation of the correlation matrix for the systems liganded with the MMRi6 inhibitor. The results show that both systems exhibit significant positive and negative correlations, with **Figures 18B and 18D** showing stronger positive correlations than **Figures 18A** and 18**C**. **Figs 18A** and 18**C** also show a strong negative correlation, with **Fig 18C** being more negative.


A
Residue Number
Residue Number
1,000
0,7500
0,5000
0,2500
0
-0,2500
-0,5000
-0,7500
-1,000
B
Residue Number
Residue Number
1.000
0.7500
0.5000
0.2500
0
-0.2500
-0.5000
-0.7500
-1.000
C
Residue Number
Residue Number
1.000
0.7500
0.5000
0.2500
0
-0.2500
-0.5000
-0.7500
-1.000

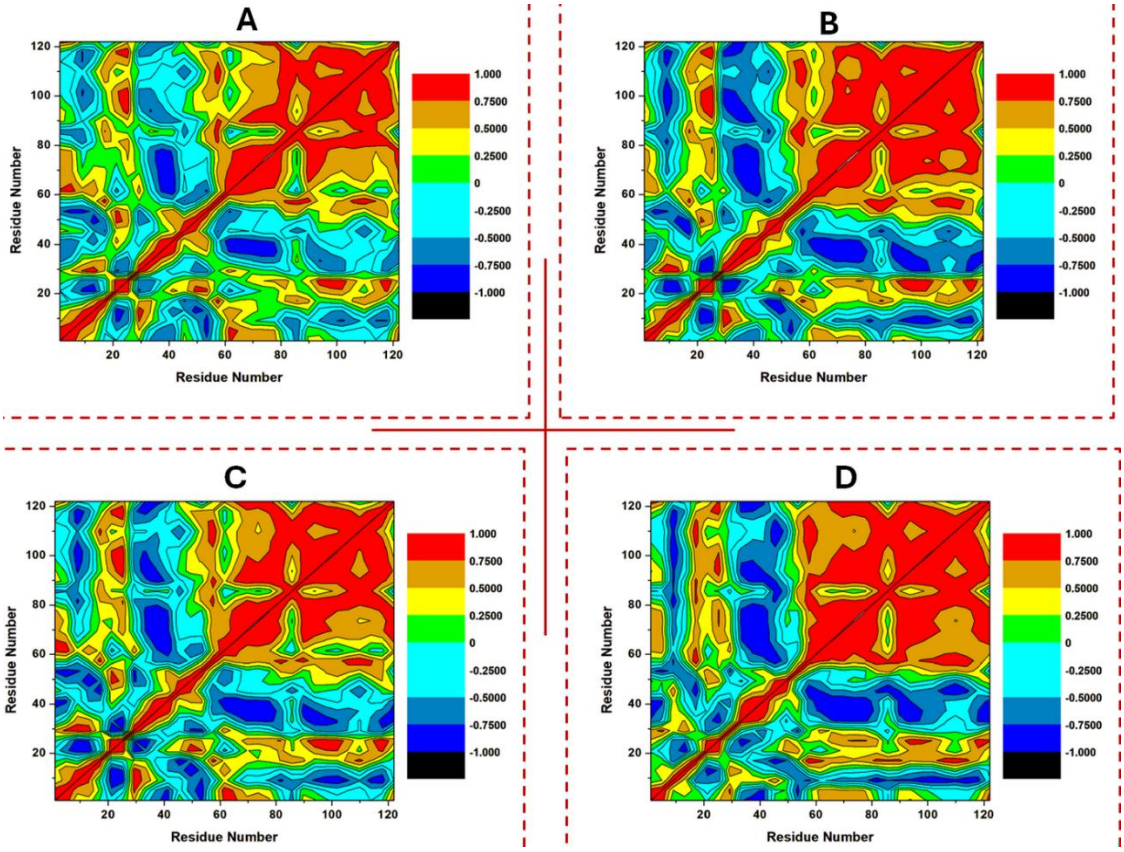


Figure 18. The DCCM systems for liganded MDM2/X protein systems with **MMRi6** taken throughout 200 ns MD simulations: (A) K478R mutation. (B) N448C mutation. (C) K478R/N448C mutations. (D) WT-liganded.

Fig. 19, on the other hand, shows the correlation matrix for the systems liganded with the MMRi64 inhibitor. From the results, **Fig. 19C** has the lowest positive correlation, **followed closely by Fig. 19A**.

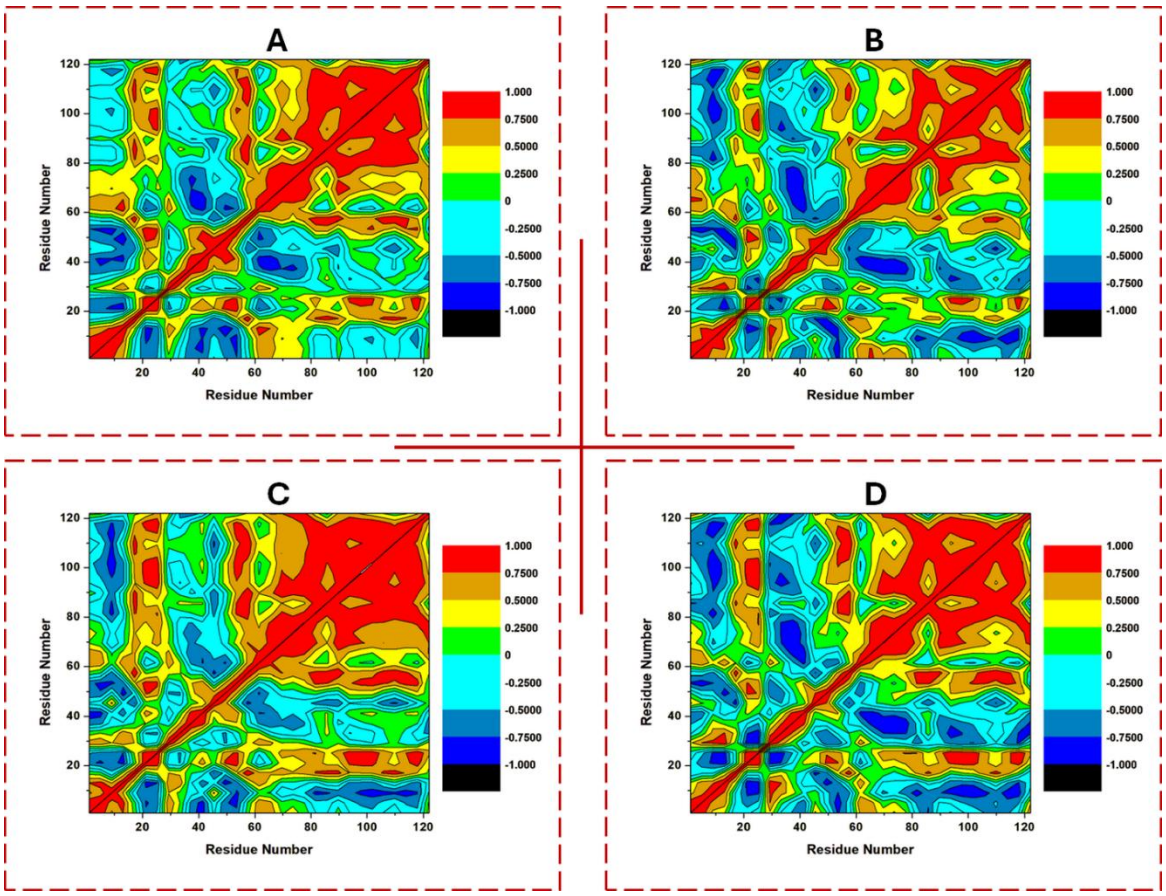


Figure 19. DSSP analysis of liganded MDM2/X protein systems with MMRi64 over 200 ns MD simulations: (A) K478R mutation. (B) N448C mutation. (C) K478R/N448C mutations. (D) WT-liganded.

3.8 *Visual conformational changes of MDM2/X RINGs* and *distance matrix*

Snapshot frames of systems were extracted from the trajectories to specifically analyse the changes in the conformation of the MDM2/X RING heterodimer interface.

The snapshots illustrated in **Fig. 20** depict the unbound (Apo) and bound secondary structure of the MDM2/X protein complex. The visual images captured at 150 ns revealed significant variations across the systems.

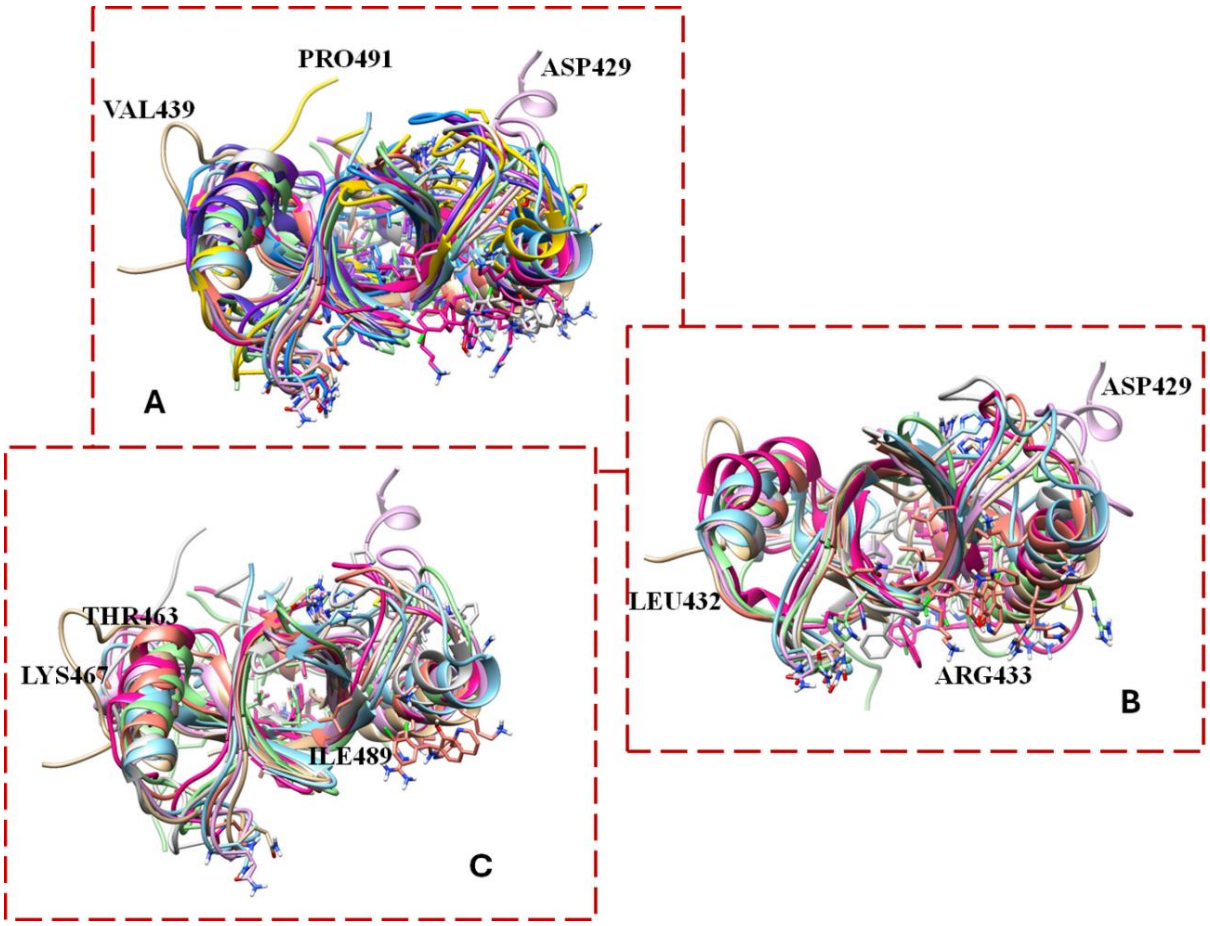


Figure 20. Snapshots showing the impact of mutations and ligand binding on the structure of the MDM2/X complex: (A) Apo, MMRi6 and MMRi64 systems. (B) Apo and MMRi6 systems. (C) Apo and MMRi64 systems.

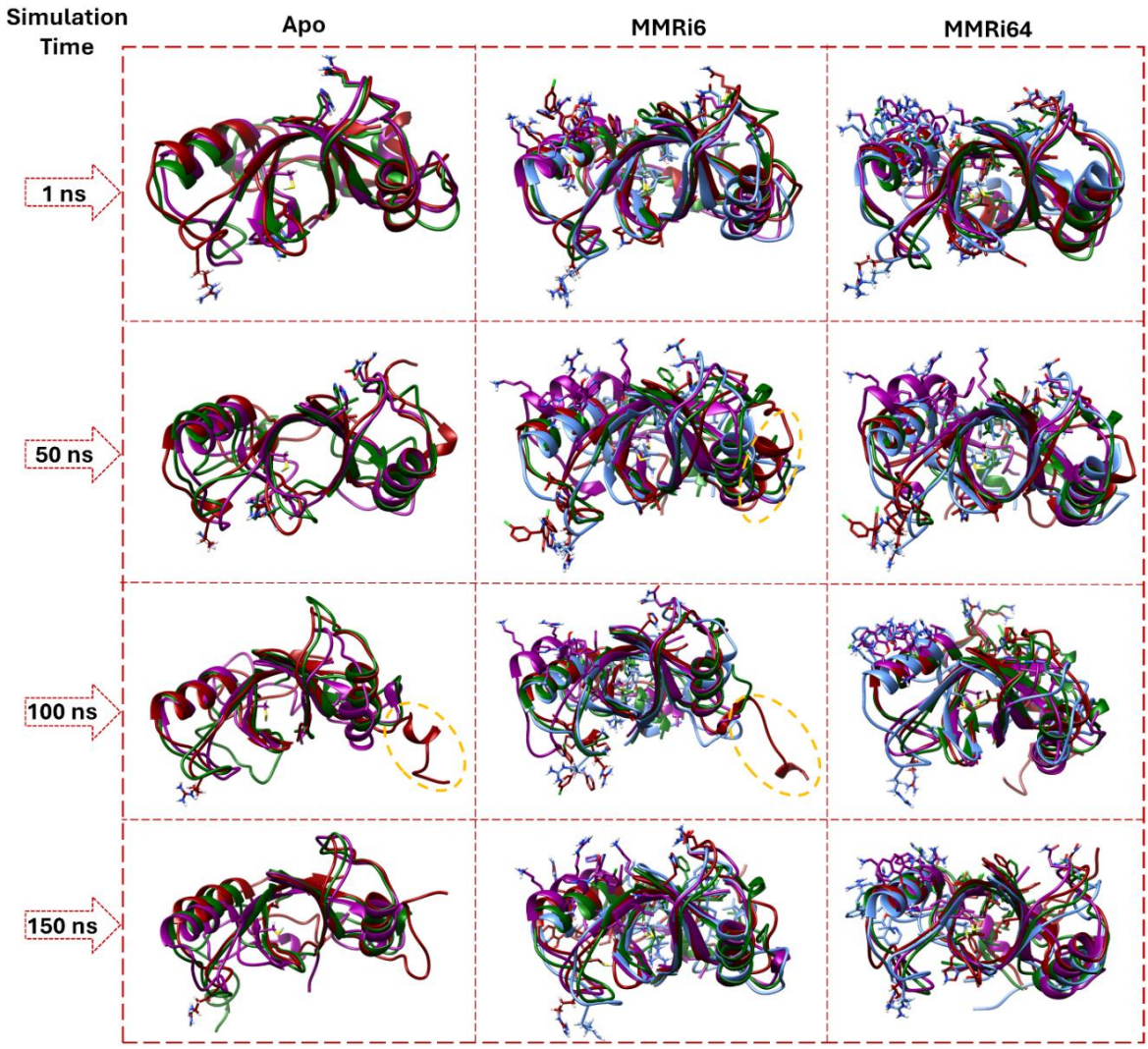


Figure 21. Representative snapshots comparing the Apo, MMRi6, and MMRi64 systems at 1, 50, 100, and 150 ns, showing the level of structural changes in the MDM2/X complex. Colour outline: WT (dark green), K478R mutated (dark red), N448C mutated (dark magenta), K478R/N448C double mutation (cornflower blue).

Protein function depends on the spatial organization of residues forming the structural framework for molecular recognition and activity. In the MDM2–MDMX RING heterodimer, maintaining

specific inter-residue contacts is crucial because ubiquitin ligase activity requires precise structural communication between the two domains. Consequently, residue–residue distance matrices reveal how mutations and inhibitor binding alter the interaction networks required for functional ubiquitination (57,76).

For the MMRi6 systems, distinct distance rearrangements occurred. In the wild-type (WT) complex, the PRO444–LEU433 distance decreased from 12.85 Å (1 ns) to 9.82 Å (150 ns), indicating local compaction. Similarly, in K478R–MMRi6, the LYS469-ARG465 distance shortened from 12.74 Å to 6.44 Å, suggesting enhanced structural coupling. Conversely, N448C-MMRi6 expanded from 7.18 Å to 10.11 Å, while the double mutant showed initial contraction followed by partial re-expansion. This demonstrates that MMRi6 remodels specific contact pathways depending on the mutational background rather than inducing a uniform response.

The MMRi64 complexes exhibited more pronounced changes. WT-MMRi64 showed PRO444-LEU433 distance expansion (8.97 Å to 12.34 Å), whereas K478R–MMRi64 displayed contraction (10.30 Å to 8.43 Å). The most significant reorganization occurred in K478R/N448C–MMRi64, where the LYS469–ARG465 distance decreased from 11.53 Å to 6.39 Å. These contractions parallel the favorable MMGBSA binding energetics, suggesting that mutation-enhanced inhibitor binding promotes alternative residue-contact arrangements. Such rearrangements are particularly significant because residue-contact networks constitute the physical pathways through which conformational information is transmitted across protein structures (77,78).

These distance matrices identify the physical rearrangements underlying the altered dynamic communication detected by DCCM, and the global/local flexibility changes captured by RMSD and RMSF. Collectively, the results indicate that mutation-enhanced inhibitor efficacy is driven by ligand-induced reconfiguration of residue communication pathways. The K478R and N448C

mutations facilitate structural rewiring of critical networks, perturbing the conformational organization required for efficient ubiquitin transfer.

Table 6. Distances between critical residues in the MDM2/X systems at different simulation times. All values are in Angstrom (Å).

		MMRi6				**MMRi64**		
Systems	**Residues**	**1 ns**	**100 ns**	**150 ns**	**Residues**	**1 ns**	**100 ns**	**150 ns**
WT	PRO444-LEU433	12.85	10.39	9.82	PRO444-LEU433	8.97	11.74	12.34
K478R	LYS469-ARG465	12.74	9.74	6.44	PRO444-LEU433	10.30	9.51	8.43
N448C	LYS469-ARG465	7.18	11.24	10.11	LYS469-ARG465	8.37	12.47	11.15
K478R/N448C	PRO444-LEU433	14.87	9.26	10.72	LYS469-ARG465	11.53	9.79	6.39

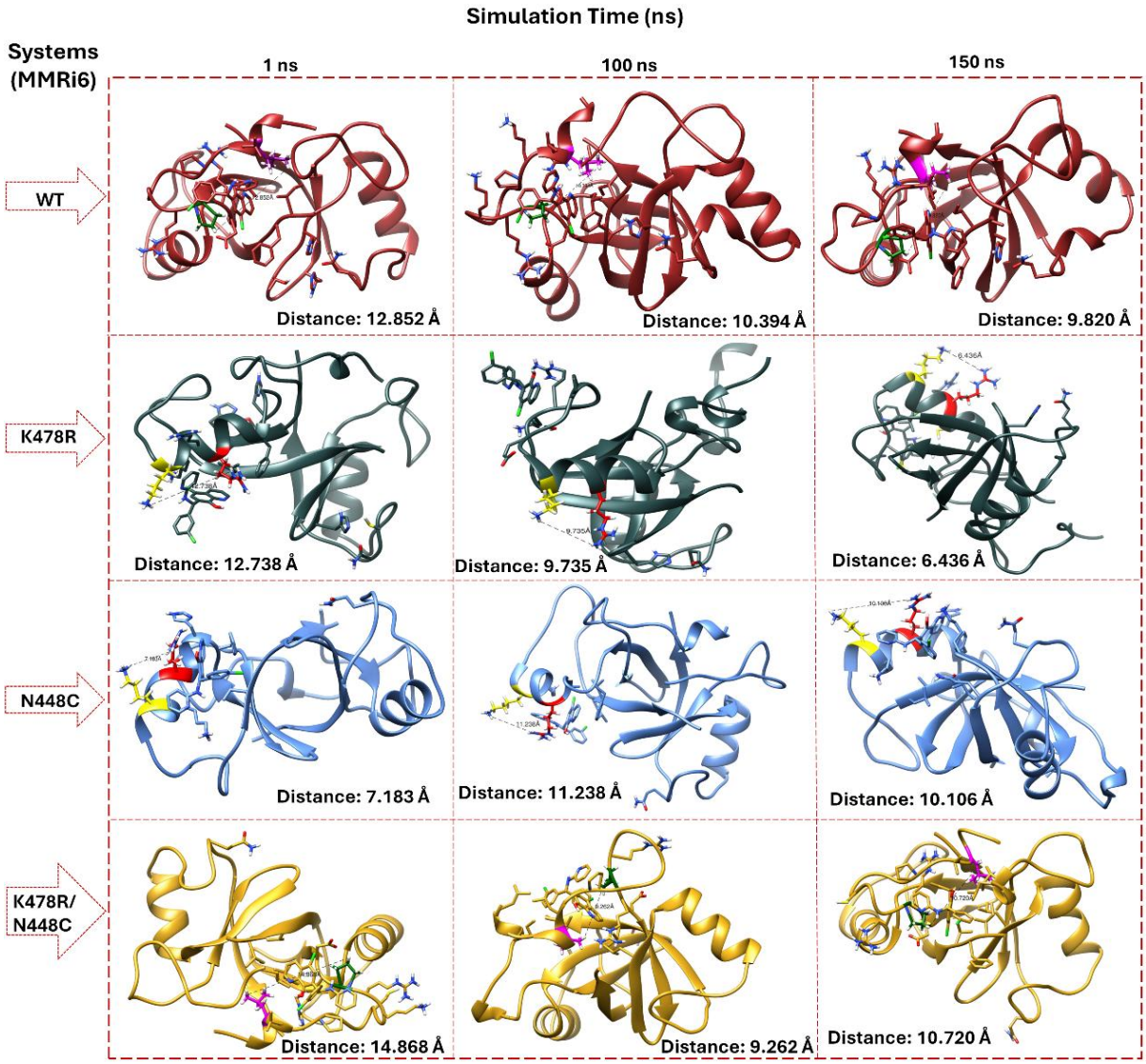


Figure 22. Estimated distances between PRO444 (dark green) and LEU433 (magenta), and LYS469 (yellow) and ARG465 (red) residues in the MMRi6-bound systems using snapshots taken at 1, 100, and 150 ns.

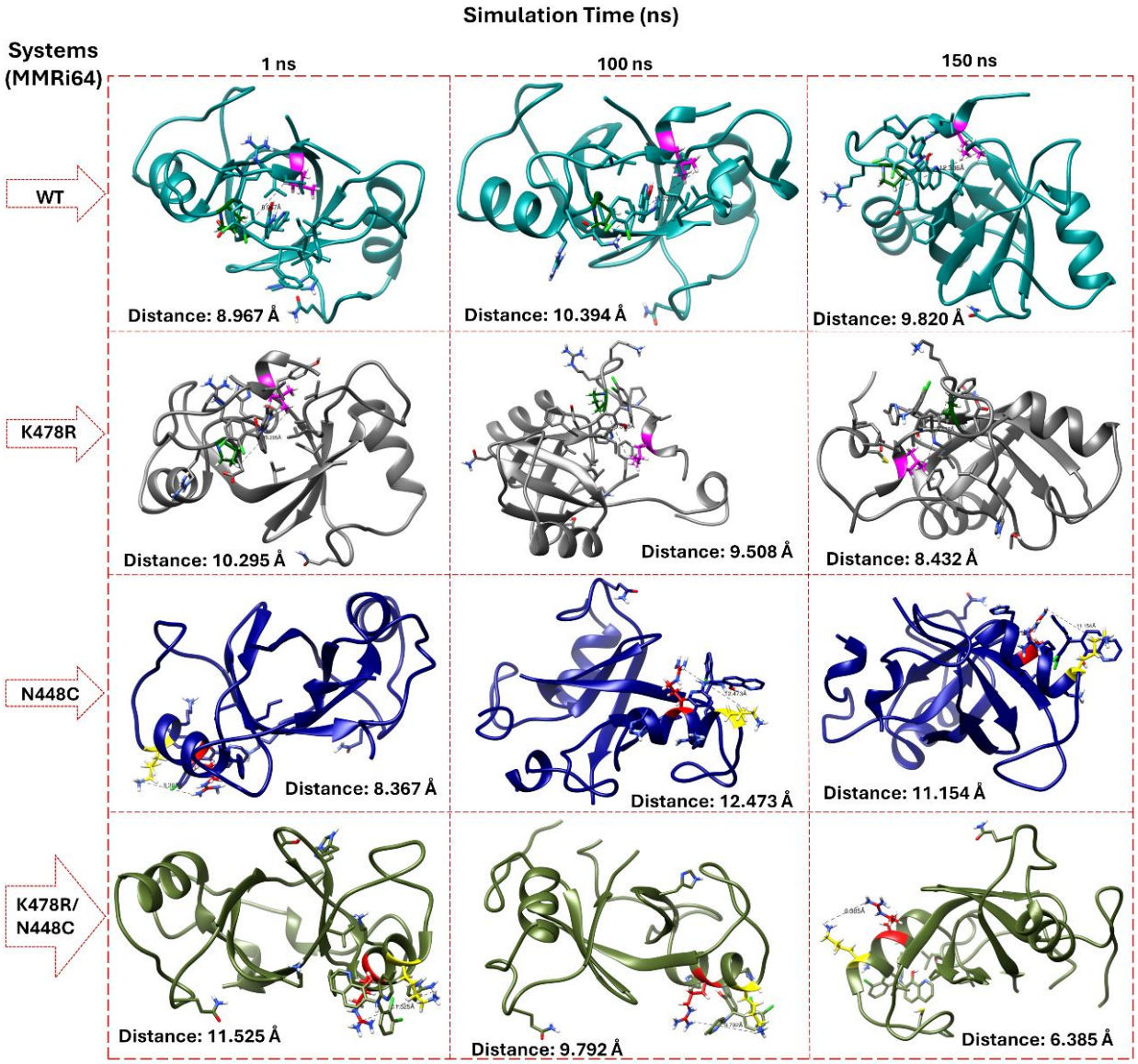


Figure 23. Estimated distances between PRO444 and LEU433 (dark green and magenta, respectively), and LYS469 and ARG465 (yellow and red, respectively) residues in the MMRi64-bound systems using snapshots taken at 1, 100, and 150 ns.

4.0 CONCLUSION

The MDM2–MDMX RING heterodimer plays a pivotal role in p53 ubiquitination and degradation, making it an attractive target for anticancer intervention. The primary objective of this study was to determine how MDMX RING domain mutations alter the structural and energetic behaviour of

the MDM2–MDMX heterodimer in the presence of small-molecule inhibitors MMRi6 and MMRi64, and how these changes influence the p53 tumor suppressor pathway. The biological mechanism emerges from the convergence of multiple analytical metrics rather than a single parameter. Collectively, the findings reveal a coherent framework in which K478R and N448C mutations remodel the energetic landscape, conformational dynamics, residue communication networks, and structural architecture of the heterodimer, enhancing inhibitor-mediated disruption.

Docking studies indicated that the mutations reshape the physicochemical environment of the binding region to accommodate both inhibitors favorably. MMGBSA calculations provided thermodynamic confirmation, showing the most favorable free-energy values in mutant systems, particularly K478R/N448C–MMRi6 and K478R–MMRi64. Per-residue energy decomposition revealed that residues PRO444, ARG465, LYS468, LYS469, LEU432, LEU433, LEU434, and ILE489 were dominant energetic contributors across multiple mutant systems. Rather than concentrating binding energy within isolated hotspots, the strongest inhibitor-bound systems distributed interactions across broader residue networks, increasing binding robustness.

Dynamic analyses (RMSD, RMSF, PCA, RoG, and SASA) demonstrated that mutation-enhanced inhibitor binding reorganizes the conformational landscape via complementary mechanisms. The N448C mutation promoted structural stabilization, solvent protection, and increased compactness. Conversely, K478R increased conformational plasticity and enabled broader structural exploration. Notably, K478R–MMRi64 simultaneously exhibited the strongest binding affinity and the largest structural deviations. This indicates that productive inhibition drives the heterodimer into alternative, functionally impaired conformational ensembles rather than simple native-state rigidification. DSSP analysis confirmed that these changes occurred without catastrophic loss of secondary structure; α-helices and β-sheets remained largely preserved across

all 200 ns simulations, distinguishing targeted allosteric regulation from nonspecific protein destabilization.

DCCM and distance matrix analyses showed extensive physical and dynamic rewiring of communication pathways. K478R promoted anti-correlated motions and network remodeling, whereas N448C strengthened local correlated interactions. Inhibitor binding amplified these altered architectures, disrupting the precise spatial alignment of the RING domains required for E2 recruitment and ubiquitin transfer.

Because MDM2–MDMX heterodimerization is indispensable for effective p53 suppression, disrupting this communication framework will reduce p53 ubiquitination and degradation. Consequently, the K478R and N448C mutations optimize the molecular environment for MMRi6 and MMRi64 activity, amplifying inhibitor efficacy to potentially restore p53 tumor suppressor function. However, because mutations cause varied structural flexibility, personalized inhibitor selection is required to overcome resistance and maximize therapeutic efficacy.

Author Contributions

Conceptualisation: A.T.A., and S.M.

Methodology: A.T.A, W. M. O., L. S., and S.M.,

Software: A.T.A., W. M. O., S. C.E., and S.M.

Validation: A.T.A, W. M. O., L. S., S. C.E., and S.M.

Formal Analysis: A.T.A, W. M. O., S. C. E., and S. M.

Writing (original draft): A.T.A., W. M. O., and S. C. E.

Writing (review): A.T.A., W. M. O., L. S., S. C.E., and S.M.

Supervision: S.M.

All authors have read and agreed to the published version of the manuscript.

Funding

The research received no external funding.

Data Availability Statement

The protein used in the experiment was retrieved from the RCSB protein data bank (RCSB PDB) (https://www.rcsb.org/structure/2VJE). The 3D MMRi6 and MMRi64 were retrieved from https://pubchem.ncbi.nlm.nih.gov/#query=MMRi64+and+MMRi6, the PubChem database. The removal of the unused protein chain, non-standard ligands, and required visualization during the study was performed using the UCSF Chimera software (https://www.cgl.ucsf.edu/chimera/). Other interactive visualization and analysis of molecular structures and related data were performed using BIOVIA DS Visualizer version 2021 (https://discover.3ds.com/discovery-studio-visualizer-download) and Molegro Molecular Viewer www.molegro.com. Autodock Vina, used for the molecular docking studies, is freely available at https://doi.org/10.1021/acs.jcim.1c00203. The molecules were optimized using Avogadro's Tool, which is made freely available at https://avogadro.cc/. The PMEMD CUDA GPU version provided with the AMBER package, available at the Centre for High-performance Computing (CHPC) in Cape Town, South Africa, was used to run the MD simulations (https://www.chpc.ac.za/) and (https://users.chpc.ac.za/). All the parameters used for the calculations in the MD simulation are provided in detail in the "Methodology" section. All data, including docking results, docking poses, MD simulation trajectories, RMSD, RMSF, RoG, PCA, PRED, MMGBSA, DCCA, Snapshots, and others, were made available at https://github.com/Jesutomisin0707/-Data-allosteric-rewiring-of-the-MDM2-MDMX-RING-interface-by-K478R-and-N448C, and the rest of the data are available at

https://github.com/Jesutomisin0707/-Allosteric-rewiring-of-the-MDM2-MDMX-RING-interface-by-K478R-and-N448C-2.

Conflicts of Interest

The authors declare no conflict.

Ethics statement

As this study relies entirely on computational simulations, molecular dynamics analysis, and *in-silico* modeling, it did not involve human participants or animal subjects. Therefore, ethical board approval and informed consent were not required.

Acknowledgment

First, the authors acknowledge the ALMIGHTY GOD who created all things, including life, wisdom, and knowledge for every human being. We thank the Centre for High-Performance Computing (CHPC, www.chpc.ac.za) for providing computational resources. Lastly, the authors appreciate the Department of Life and Consumer Sciences and the University of South Africa at large for providing funding for this postdoctoral fellowship and for their other support.

REFERENCES

1. Chhikara BS, Parang Keykavous. Global Cancer Statistics 2022: the trends projection analysis. Chemical Biology Letters [Internet]. 2023 Jan 2 [cited 2026 Jan 13];10(1):451. Available from: https://pubs.thesciencein.org/journal/index.php/cbl/article/view/451
2. Siegel RL, Kratzer TB, Giaquinto AN, Sung H, Jemal A. Cancer statistics, 2025. CA Cancer J Clin. 2025 Jan 16;75(1):10–45. doi:10.3322/caac.21871
3. Nussinov R, Tsai CJ, Jang H. Anticancer drug resistance: An update and perspective. Drug Resistance Updates. 2021 Dec;59:100796. doi:10.1016/j.drup.2021.100796
4. Wang H, Guo M, Wei H, Chen Y. Targeting p53 pathways: mechanisms, structures and advances in therapy. Signal Transduct Target Ther. 2023 Mar 1;8(1):92. doi:10.1038/s41392-023-01347-1

5. Patil MR, Bihari A. A comprehensive study of p53 protein. J Cell Biochem. 2022 Dec 2;123(12):1891–937. doi:10.1002/jcb.30331

6. Kim KM, Ahn AR, Park HS, Jang KY, Moon WS, Kang MJ, et al. Clinical significance of p53 protein expression and TP53 variation status in colorectal cancer. BMC Cancer. 2022 Aug 31;22(1):940. doi:10.1186/s12885-022-10039-y

7. Wang W, Albadari N, Du Y, Fowler JF, Sang HT, Xian W, et al. MDM2 Inhibitors for Cancer Therapy: The Past, Present, and Future. Pharmacol Rev. 2024 May;76(3):414–53. doi:10.1124/pharmrev.123.001026

8. Berke TP, Slight SH, Hyder SM. Role of Reactivating Mutant p53 Protein in Suppressing Growth and Metastasis of Triple-Negative Breast Cancer. Onco Targets Ther. 2022 Jan;Volume 15:23–30. doi:10.2147/OTT.S342292

9. Gomes AS, Ramos H, Inga A, Sousa E, Saraiva L. Structural and Drug Targeting Insights on Mutant p53. Cancers (Basel). 2021 Jul 3;13(13):3344. doi:10.3390/cancers13133344

10. Zhu IY, Lloyd A, Critchley WR, Saikia Q, Jade D, Divan A, et al. Structure and function of MDM2 and MDM4 in health and disease. Biochemical Journal. 2025 Feb 19;482(04):241–62. doi:10.1042/BCJ20240757

11. Ballarotto M, Bianconi E, Valentini S, Temperini A, Moretti F, Macchiarulo A. Rational design, synthesis, and biophysical characterization of a peptidic MDM2-MDM4 interaction inhibitor. Bioorg Med Chem. 2024 Nov;113:117937. doi:10.1016/j.bmc.2024.117937

12. Klein AM, de Queiroz RM, Venkatesh D, Prives C. The roles and regulation of MDM2 and MDMX: it is not just about p53. Genes Dev. 2021 May 1;35(9–10):575–601. doi:10.1101/gad.347872.120

13. Wei Q, Li C, Tang Y, Bai J, Li W, Liu J, et al. Mechanistic Role of the Mdm2/MdmX Lid Domain in Regulating Their Interactions with p53. Biomolecules. 2025 Apr 30;15(5):642. doi:10.3390/biom15050642

14. Xiong S, Zhang Y, Zhou X, Pant V, Mirani A, Gencel-Augusto J, et al. Dependence on Mdm2 for Mdm4 inhibition of p53 activity. Cancer Lett. 2025 Jul;621:217622. doi:10.1016/j.canlet.2025.217622

15. Lama R, Fose JM, Martín D, Muñoz IG, Wang ES, Sung PJ, et al. Novel Inhibitors for MDM2-MDM4 E3 Ligase Potently Induce p53-Independent Apoptosis in Drug-Resistant Leukemic Cells. Molecules. 2025 Jan 5;30(1):186. doi:10.3390/molecules30010186

16. Ilic VK, Egorova O, Tsang E, Gatto M, Wen Y, Zhao Y, et al. Hinokiflavone Inhibits MDM2 Activity by Targeting the MDM2-MDMX RING Domain. Biomolecules. 2022 Apr 27;12(5):643. doi:10.3390/biom12050643

17. Wu W, Xu C, Ling X, Fan C, Buckley BP, Chernov M V, et al. Targeting RING domains of Mdm2–MdmX E3 complex activates apoptotic arm of the p53 pathway in

leukemia/lymphoma cells. Cell Death Dis. 2015 Dec 31;6(12):e2035–e2035. doi:10.1038/cddis.2015.358

18. Attili M, Valentini S, Pesavento M, Ballarotto M, Scognamiglio V, Pontecorvi A, et al. Exploring the heterodimer MDM2/MDM4 interaction region uncovers high-affinity peptides for therapeutic p53-reactivation. Frontiers in Chemical Biology. 2025 May 12;4. doi:10.3389/fchbi.2025.1576640

19. Kosztyu P, Slaninová I, Valčíková B, Verlande A, Müller P, Paleček JJ, et al. A Single Conserved Amino Acid Residue as a Critical Context-Specific Determinant of the Differential Ability of Mdm2 and MdmX RING Domains to Dimerize. Front Physiol [Internet]. 2019;Volume 10-2019. Available from: https://www.frontiersin.org/journals/physiology/articles/10.3389/fphys.2019.00390

20. Egorova O, Sheng Y. A site-directed mutagenesis study of the MdmX RING domain. Biochem Biophys Res Commun. 2014;447(4):696–701. doi:https://doi.org/10.1016/j.bbrc.2014.04.065

21. Yanga Z, Keren Laskerb, Dina Schneidman-Duhovny, Ben Webb, Conrad C. Huang, Eric F. Pettersen, Thomas D. Goddard, Elaine C. Meng, Andrej Sali and TEF. UCSF Chimera, MODELLER, and IMP: an Integrated Modeling System. J Struct Biol. 2012;23(1):1–7. doi:10.1038/jid.2014.371 PubMed PMID: 1000000221.

22. Pettersen EF, Goddard TD, Huang CC, Couch GS, Greenblatt DM, Meng EC, et al. UCSF Chimera — A Visualization System for Exploratory Research and Analysis. J Comput Chem. 2004;25(13):1605–12. doi:10.1002/jcc.20084

23. Adewumi AT, Oluyemi WM, Adekunle YA, Adewumi N, Alahmdi MI, Soliman MES, et al. Propitious Indazole Compounds as β-ketoacyl-ACP Synthase Inhibitors and Mechanisms Unfolded for TB Cure: Integrated Rational Design and MD Simulations. ChemistrySelect. 2023 Jan 23;8(3). doi:10.1002/slct.202203877

24. Tian W, Chen C, Lei X, Zhao J, Liang J. CASTp 3.0: computed atlas of surface topography of proteins. Nucleic Acids Res. 2018 Jul 2;46(W1):W363–7. doi:10.1093/nar/gky473

25. Ni B, Wang H, Khalaf HKS, Blay V, Houston DR. AutoDock-SS: AutoDock for Multiconformational Ligand-Based Virtual Screening. J Chem Inf Model. 2024 May 13;64(9):3779–89. doi:10.1021/acs.jcim.4c00136

26. Ciccone L, Petrarolo G, Barsuglia F, Fruchart-Gaillard C, Cassar Lajeunesse E, Adewumi AT, et al. Nature-Inspired O-Benzyl Oxime-Based Derivatives as New Dual-Acting Agents Targeting Aldose Reductase and Oxidative Stress. Biomolecules. 2022 Mar 14;12(3):448. doi:10.3390/biom12030448

27. Adewumi AT, Soremekun OS, Ajadi MB, Soliman MES. Thompson loop: opportunities for antitubercular drug design by targeting the weak spot in demethylmenaquinone methyltransferase protein. RSC Adv. 2020;10(39):23466–83. doi:10.1039/D0RA03206A

28. Florová P, Sklenovský P, Banáš P, Otyepka M. Explicit Water Models Affect the Specific Solvation and Dynamics of Unfolded Peptides While the Conformational Behavior and Flexibility of Folded Peptides Remain Intact. J Chem Theory Comput. 2010 Nov 9;6(11):3569–79. doi:10.1021/ct1003687

29. Ryckaert JP, Ciccotti G, Berendsen HJC. Numerical integration of the cartesian equations of motion of a system with constraints: molecular dynamics of n-alkanes. J Comput Phys. 1977;23(3):327–41. doi:https://doi.org/10.1016/0021-9991(77)90098-5

30. Kannan S, Partridge AW, Lane DP, Verma CS. The Dual Interactions of p53 with MDM2 and p300: Implications for the Design of MDM2 Inhibitors. Int J Mol Sci. 2019 Nov 28;20(23):5996. doi:10.3390/ijms20235996

31. Gapsys V, Michielssens S, Peters JH, de Groot BL, Leonov H. Calculation of Binding Free Energies. In. 2015. p. 173–209. doi:10.1007/978-1-4939-1465-4_9

32. Adewumi AT, Elrashedy A, Soremekun OS, Ajadi MB, Soliman MES. Weak spots inhibition in the Mycobacterium tuberculosis antigen 85C target for antitubercular drug design through selective irreversible covalent inhibitor-SER124. J Biomol Struct Dyn. 2022;40(7):2934–54. doi:10.1080/07391102.2020.1844061 PubMed PMID: 33155529.

33. Lin W, Yan Y, Huang Q, Zheng D. MDMX in Cancer: A Partner of p53 and a p53-Independent Effector. Biologics. 2024;18:61–78. doi:10.2147/BTT.S436629 PubMed PMID: 38318098.

34. Yao Y, Zhang Q, Li Z, Zhang H. MDM2: current research status and prospects of tumor treatment. Cancer Cell International. BioMed Central Ltd; 2024. doi:10.1186/s12935-024-03356-8

35. Peuget S, Zhou X, Selivanova G. Translating p53-based therapies for cancer into the clinic. Nature Reviews Cancer 2024 24:3. 2024 Jan 29;24(3):192–215. doi:10.1038/s41568-023-00658-3 PubMed PMID: 38287107.

36. Yin Q, Hu Y, Dong Z, Lu J, Wang H. Cellular, Structural Basis, and Recent Progress for Targeting Murine Double Minute X (MDMX) in Tumors. J Med Chem. 2024 Sep 12;67(17):14723–41. doi:10.1021/ACS.JMEDCHEM.4C00913 PubMed PMID: 39185935.

37. Gupta MN, Uversky VN. Biological importance of arginine: A comprehensive review of the roles in structure, disorder, and functionality of peptides and proteins. Int J Biol Macromol. 2024 Feb 1;257:128646. doi:10.1016/J.IJBIOMAC.2023.128646 PubMed PMID: 38061507.

38. Negi I, Jangra R, Gharu A, Trant JF, Sharma P. Guanidinium–amino acid hydrogen-bonding interactions in protein crystal structures: implications for guanidinium-induced protein denaturation. Physical Chemistry Chemical Physics. 2022 Dec 21;25(1):857–69. doi:10.1039/D2CP04943K PubMed PMID: 36512335.

39. Nomura K, Klejnot M, Kowalczyk D, Hock AK, Sibbet GJ, Vousden KH, et al. Structural analysis of MDM2 RING separates degradation from regulation of p53 transcription activity. Nat Struct Mol Biol. 2017 Jul 1;24(7):578. doi:10.1038/NSMB.3414 PubMed PMID: 28553961.

40. Egorova O, Sheng Y. A site-directed mutagenesis study of the MdmX RING domain. Biochem Biophys Res Commun. 2014 May 16;447(4):696–701. doi:10.1016/J.BBRC.2014.04.065 PubMed PMID: 24755078.

41. Oluyemi WM, Samuel BB, Adewumi AT, Adekunle YA, Soliman MES, Krenn L. An Allosteric Inhibitory Potential of Triterpenes from Combretum racemosum on the Structural and Functional Dynamics of Plasmodium falciparum Lactate Dehydrogenase Binding Landscape. Chem Biodivers. 2022 Feb 1;19(2). doi:10.1002/cbdv.202100646 PubMed PMID: 34982514.

42. Wei Q, Li C, Tang Y, Bai J, Li W, Liu J, et al. Mechanistic Role of the Mdm2/MdmX Lid Domain in Regulating Their Interactions with p53. Biomolecules. 2025 May 1;15(5). doi:10.3390/BIOM15050642 PubMed PMID: 40427535.

43. Oluyemi WM, Nwokebu G, Adewumi AT, Eze SC, Mbachu CC, Ogueli EC, et al. The characteristic structural and functional dynamics of P. falciparum DHFR binding with pyrimidine chemotypes implicate malaria therapy design. Chemical Physics Impact. 2024 Dec 1;9. doi:10.1016/j.chphi.2024.100703

44. Yu DH, Xu ZY, Mo S, Yuan L, Cheng XD, Qin JJ. Targeting MDMX for Cancer Therapy: Rationale, Strategies, and Challenges. Front Oncol. 2020 Aug 5;10:1389. doi:10.3389/fonc.2020.01389 PubMed PMID: 32850448.

45. Wade M, Li YC, Wahl GM. MDM2, MDMX and p53 in oncogenesis and cancer therapy. Nat Rev Cancer. 2013 Feb;13(2):83–96. doi:10.1038/NRC3430 PubMed PMID: 23303139.

46. Storer MC, Hunter CA. The surface site interaction point approach to non-covalent interactions. Chemical Society Reviews. Royal Society of Chemistry; 2022. p. 10064–82. doi:10.1039/d2cs00701k PubMed PMID: 36412990.

47. Wang S, Sun X, Cui W, Yuan S. MM/PB(GB)SA benchmarks on soluble proteins and membrane proteins. Front Pharmacol. 2022 Dec 1;13:1018351. doi:10.3389/FPHAR.2022.1018351/TEXT

48. Yu Y, Wang Z, Wang L, Tian S, Hou T, Sun H. Predicting the mutation effects of protein–ligand interactions via end-point binding free energy calculations: strategies and analyses. Journal of Cheminformatics 2022 14:1. 2022 Aug 20;14(1):56-. doi:10.1186/S13321-022-00639-Y

49. Ilic VK, Egorova O, Tsang E, Gatto M, Wen Y, Zhao Y, et al. Hinokiflavone Inhibits MDM2 Activity by Targeting the MDM2-MDMX RING Domain. Biomolecules. 2022 May 1;12(5). doi:10.3390/BIOM12050643 PubMed PMID: 35625571.

50. Ramli I, Cheriet T, Posadino AM, Giordo R, Fenu G, Chukwuemeka Nwachukwu K, et al. Modulating the p53-MDM2 pathway: the therapeutic potential of natural compounds in cancer treatment. EXCLI J. 2024 Jan 3;23:1397–439. doi:10.17179/excli2024-7791 PubMed PMID: 39764218.

51. Linke K, Mace PD, Smith CA, Vaux DL, Silke J, Day CL. Structure of the MDM2/MDMX RING domain heterodimer reveals dimerization is required for their ubiquitylation in trans. Cell Death & Differentiation 2008 15:5. 2008 Jan 25;15(5):841–8. doi:10.1038/sj.cdd.4402309 PubMed PMID: 18219319.

52. Xia M, Knezevic D, Tovar C, Huang B, Heimbrook DC, Vassilev LT. Elevated MDM2 boosts the apoptotic activity of p53-MDM2 binding inhibitors by facilitating MDMX degradation. Cell Cycle. 2008 Jun 1;7(11):1604–12. doi:10.4161/cc.7.11.5929 PubMed PMID: 18520179.

53. Genheden S, Ryde U. The MM/PBSA and MM/GBSA methods to estimate ligand-binding affinities. Expert Opin Drug Discov. 2015 May 1;10(5):449–61. doi:10.1517/17460441.2015.1032936 PubMed PMID: 25835573.

54. Danielson J; A;, Tasnim A;, Zhang JT;, Zou Y;, Liu JY, Seidman M, et al. Proline Isomerization: From the Chemistry and Biology to Therapeutic Opportunities. Biology 2023, Vol 12, Page 1008. 2023 Jul 14;12(7):1008. doi:10.3390/BIOLOGY12071008 PubMed PMID: 37508437.

55. Umumararungu T, Gahamanyi N, Mukiza J, Habarurema G, Katandula J, Rugamba A, et al. Proline, a unique amino acid whose polymer, polyproline II helix, and its analogues are involved in many biological processes: a review. Amino Acids 2024 56:1. 2024 Aug 25;56(1):50-. doi:10.1007/S00726-024-03410-9 PubMed PMID: 39182198.

56. Chauhan VM, Pantazes RJ. Analysis of conformational stability of interacting residues in protein binding interfaces. Protein Eng Des Sel. 2023;36. doi:10.1093/PROTEIN/GZAD016 PubMed PMID: 37889566.

57. Hung TI, Hsieh YJ, Lu WL, Wu KP, Chang C en A. What Strengthens Protein-Protein Interactions: Analysis and Applications of Residue Correlation Networks. J Mol Biol. 2023 Dec 15;435(24). doi:10.1016/j.jmb.2023.168337 PubMed PMID: 37918563.

58. Liu K, Watanabe E, Kokubo H. Exploring the stability of ligand binding modes to proteins by molecular dynamics simulations. J Comput Aided Mol Des. 2017 Feb 1;31(2):201–11. doi:10.1007/s10822-016-0005-2 PubMed PMID: 28074360.

59. Hollingsworth SA, Dror RO. Molecular Dynamics Simulation for All. Neuron. 2018 Sep 19;99(6):1129–43. doi:10.1016/j.neuron.2018.08.011 PubMed PMID: 30236283.

60. Zhu J, Wang J, Han W, Xu D. Neural relational inference to learn long-range allosteric interactions in proteins from molecular dynamics simulations. Nature Communications 2022 13:1. 2022 Mar 29;13(1):1661-. doi:10.1038/s41467-022-29331-3 PubMed PMID: 35351887.

61. Ni D, Liu Y, Kong R, Yu Z, Lu S, Zhang J. Computational elucidation of allosteric communication in proteins for allosteric drug design. Drug Discov Today. 2022 Aug 1;27(8):2226–34. doi:10.1016/j.drudis.2022.03.012 PubMed PMID: 35314339.

62. Wang J, Arantes PR, Bhattarai A, Hsu R V., Pawnikar S, Huang Y ming M, et al. Gaussian accelerated molecular dynamics (GaMD): principles and applications. Wiley Interdiscip Rev Comput Mol Sci. 2021 Sep 1;11(5). doi:10.1002/WCMS.1521 PubMed PMID: 34899998.

63. Gunasinghe J, Abu Talib MI, Cheah S, Runnie Ginjom I, Lee SH, Chee XW. Discovery of inhibitors of MDM2 against nasopharyngeal cancer: An in-silico investigation. Journal of Smart Science and Technology. 2023;2(3):44–56.

64. Verkhivker GM. Making the invisible visible: Toward structural characterization of allosteric states, interaction networks, and allosteric regulatory mechanisms in protein kinases. Curr Opin Struct Biol. 2021 Dec 1;71:71–8. doi:10.1016/J.SBI.2021.06.002 PubMed PMID: 34237520.

65. Nussinov R, Tsai CJ. Allostery in disease and in drug discovery. Cell. 2013 Apr 11;153(2):293–305. doi:10.1016/j.cell.2013.03.034 PubMed PMID: 23582321.

66. Papaleo E, Saladino G, Lambrughi M, Lindorff-Larsen K, Gervasio FL, Nussinov R. The Role of Protein Loops and Linkers in Conformational Dynamics and Allostery. Chem Rev. 2016 Jun 8;116(11):6391–423. doi:10.1021/ACS.CHEMREV.5B00623 PubMed PMID: 26889708.

67. Adewumi AT, Soremekun OS, Ajadi MB, Soliman MES. Thompson loop: opportunities for antitubercular drug design by targeting the weak spot in demethylmenaquinone methyltransferase protein. RSC Adv. 2020 Jun 16;10(39):23466–83. doi:10.1039/d0ra03206a PubMed PMID: 35520325.

68. Altis A, Nguyen PH, Hegger R, Stock G. Dihedral angle principal component analysis of molecular dynamics simulations. J Chem Phys. 2007 Jun 29;126(24):244111. doi:10.1063/1.2746330

69. Nussinov R, Tsai CJ, Ma B. The underappreciated role of allostery in the cellular network. Annu Rev Biophys. 2013 May;42(1):169–89. doi:10.1146/ANNUREV-BIOPHYS-083012-130257 PubMed PMID: 23451894.

70. Pei D, Zhang Y, Zheng J. Regulation of p53: A collaboration between Mdm2 and Mdmx. Oncotarget. 2012;3(3):228–35. doi:10.18632/oncotarget.443 PubMed PMID: 22410433.

71. Zhang D, Lazim R. Application of conventional molecular dynamics simulation in evaluating the stability of apomyoglobin in urea solution. Sci Rep. 2017;7(1):44651. doi:10.1038/srep44651

72. Wang S, Sun X, Cui W, Yuan S. MM/PB(GB)SA benchmarks on soluble proteins and membrane proteins. Front Pharmacol. 2022 Dec 1;13. doi:10.3389/fphar.2022.1018351

73. Hekkelman ML, Salmoral DÁ, Perrakis A, Joosten RP. DSSP 4: FAIR annotation of protein secondary structure. Protein Science. 2025 Aug 1;34(8):e70208. doi:https://doi.org/10.1002/pro.70208

74. Hertig S, Latorraca NR, Dror RO. Revealing Atomic-Level Mechanisms of Protein Allostery with Molecular Dynamics Simulations. PLoS Comput Biol. 2016 Jun 1;12(6). doi:10.1371/journal.pcbi.1004746 PubMed PMID: 27285999.

75. Okamoto C, Ando K. Molecular dynamics simulation analysis of structural dynamic cross correlation induced by odorant hydrogen-bonding in mouse eugenol ol- factory receptor. Biophys Physicobiol. 2024;21(1). doi:10.2142/biophysico.bppb-v21.0007

76. Petrizzelli F, Biagini T, Bianco SD, Liorni N, Napoli A, Castellana S, et al. Connecting the dots: A practical evaluation of web-tools for describing protein dynamics as networks. Frontiers in Bioinformatics. 2022 Oct 19;2:1045368. doi:10.3389/FBINF.2022.1045368/TEXT

77. Dubanevics I, McLeish TCB. Optimising Elastic Network Models for Protein Dynamics and Allostery: Spatial and Modal Cut-offs and Backbone Stiffness. J Mol Biol. 2022 Sep 15;434(17). doi:10.1016/j.jmb.2022.167696 PubMed PMID: 35810792.

78. Schneider M, Antes I. SenseNet, a tool for analysis of protein structure networks obtained from molecular dynamics simulations. PLoS One. 2022 Mar 1;17(3). doi:10.1371/JOURNAL.PONE.0265194 PubMed PMID: 35298511.